Atmospheric
Chemistry
and Physics

Determination of the absorption cross sections of higher-order iodine oxides at 355 and 532 nm

Thomas R. Lewis[1,2], **Juan Carlos Gómez Martín**[3], **Mark A. Blitz**[2], **Carlos A. Cuevas**[1], **John M. C. Plane**[2], and **Alfonso Saiz-Lopez**[1]

[1]Department of Atmospheric Chemistry and Climate, Institute of Physical Chemistry Rocasolano, CSIC, Madrid, Spain
[2]School of Chemistry, University of Leeds, LS29JT, Leeds, UK
[3]Instituto de Astrofísica de Andalucía, CSIC, 18008, Granada, Spain

Correspondence: Juan Carlos Gómez Martín (jcgomez@iaa.es), John M. C. Plane (j.m.c.plane@leeds.ac.uk) and Alfonso Saiz-López (a.saiz@csic.es)
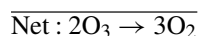
Abstract. Iodine oxides (I_xO_y) play an important role in the atmospheric chemistry of iodine. They are initiators of new particle formation events in the coastal and polar boundary layers and act as iodine reservoirs in tropospheric ozone-depleting chemical cycles. Despite the importance of the aforementioned processes, the photochemistry of these molecules has not been studied in detail previously. Here, we report the first determination of the absorption cross sections of I_xO_y, $x = 2, 3, 5$, $y = 1$–12 at $\lambda = 355$ nm by combining pulsed laser photolysis of I_2/O_3 gas mixtures in air with time-resolved photo-ionization time-of-flight mass spectrometry, using NO_2 actinometry for signal calibration. The oxides selected for absorption cross-section determinations are those presenting the strongest signals in the mass spectra, where signals containing four iodine atoms are absent. The method is validated by measuring the absorption cross section of IO at 355 nm, $\sigma_{355\,nm,\,IO} = (1.2 \pm 0.1) \times 10^{-18}$ cm^2, which is found to be in good agreement with the most recent literature. The results obtained are $\sigma_{355\,nm,\,I2O3} < 5 \times 10^{-19}$ cm^2 molec.$^{-1}$, $\sigma_{355\,nm,\,I2O4} = (3.9 \pm 1.2) \times 10^{-18}$ cm^2 molec.$^{-1}$, $\sigma_{355\,nm,\,I3O6} = (6.1 \pm 1.6) \times 10^{-18}$ cm^2 molec.$^{-1}$, $\sigma_{355\,nm,\,I3O7} = (5.3 \pm 1.4) \times 10^{-18}$ cm^2 molec.$^{-1}$, and $\sigma_{355\,nm,\,I5O12} = (9.8 \pm 1.0) \times 10^{-18}$ cm^2 molec.$^{-1}$. Photodepletion at $\lambda = 532$ nm was only observed for OIO, which enabled determination of upper limits for the absorption cross sections of I_xO_y at 532 nm using OIO as an actinometer. These measurements are supplemented with ab initio calculations of electronic spectra in order to estimate atmospheric photolysis rates $J(I_xO_y)$. Our results confirm a high $J(I_xO_y)$ scenario where I_xO_y is efficiently removed during daytime, implying enhanced iodine-driven ozone depletion and hindering iodine particle formation. Possible I_2O_3 and I_2O_4 photolysis products are discussed, including IO_3, which may be a precursor to iodic acid (HIO_3) in the presence of HO_2.
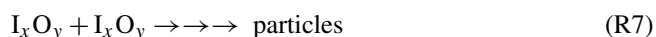
1 Introduction

Photolabile iodine-containing molecules are emitted into the lower atmosphere from the sea surface and from marine biota. The atmospheric processing of iodine leads to its accumulation in aerosol and subsequent transport and deposition on land, where it enters the continental ecosystems (Saiz-Lopez et al., 2012b). In the course of this process, gas-phase reactive iodine is involved in two important chemical processes of the background troposphere: ozone depletion and new particle formation. Iodine is thought to be responsible for 9 to 16 % of the contemporary ozone removal in the tropical troposphere (Saiz-Lopez et al., 2014; Sherwen et al., 2016), and there is evidence that anthropogenic ozone pollution enhances iodine release from the sea surface (Carpenter et al., 2013; Chance et al., 2014; MacDonald et al., 2014; Prados-Roman et al., 2015; Cuevas et al., 2018), which in turn has accelerated ozone loss in the last decades (Cuevas et al., 2018). The atmospheric chemistry of iodine is in principle fairly simple, since the main atmospheric fate of the

iodine atoms is reaction with ozone to form iodine monoxide (IO). This radical photolyses readily (Gómez Martín et al., 2005), creating an ozone-neutral cycle and establishing a steady-state concentration of I and IO, which are then termed collectively active iodine or IO_x. Any other chemical cycle involving IO which recycles atomic iodine without concomitant generation of atomic oxygen leads to ozone depletion, e.g. (Gómez Martín et al., 2009):

$$I + O_3 \rightarrow IO + O_2 \tag{R1}$$
$$IO + IO \rightarrow OIO + I \tag{R2}$$
$$OIO + hv \rightarrow I + O_2 \tag{R3}$$

$$\overline{Net : 2O_3 \rightarrow 3O_2}$$

Further steps in this scheme lead to the formation of higher iodine oxides (Gómez Martín et al., 2013).

$$IO + IO \rightarrow I_2O_2 \tag{R4}$$
$$IO + OIO \rightarrow I_2O_3 \tag{R5}$$
$$OIO + OIO \rightarrow I_2O_4 \tag{R6}$$
$$I_xO_y + I_xO_y \rightarrow \rightarrow \rightarrow \text{ particles} \tag{R7}$$

Previous laboratory experiments on iodine photochemistry have reported kinetic growth of broadband absorptions following the decay of IO and OIO as well as significant deposition of particulates on the walls of the reactors (Cox and Coker, 1983; Laszlo et al., 1995; Harwood et al., 1997; Gómez Martín et al., 2005). These broadband absorbers have been tentatively identified as some of the higher iodine oxides produced in Reactions (R4), (R5), and (R6) (Bloss et al., 2001; Gómez Martín et al., 2007), which are believed to be precursors to the particles that eventually deposit on the walls. Furthermore, iodine-oxide-containing particles have been observed in multiple aerosol flow tube and steady-state chamber experiments starting from the photooxidation of iodine precursors directly injected into the chamber (Hoffmann et al., 2001; Jimenez et al., 2003; Saunders et al., 2010; Wei et al., 2017) or emitted from cultures of algae under oxidative stress (McFiggans et al., 2004; Pirjola et al., 2005). Emissions of I_2 and alkyl iodides from coastal macroalgae and polar phytoplankton and concurrent observation of IO and OIO (Saiz-Lopez and Plane, 2004) have been unambiguously linked to intense new particle formation events (Jimenez et al., 2003; McFiggans et al., 2004). Thus, there is a strong indication that iodine oxide clustering also happens in the coastal boundary layer and is responsible for particle formation events.

Recent nitrate ion chemical ionization–atmospheric pressure interface–time-of-flight mass spectrometry (NO_3^- CI-API-ToF-MS) observations of IO_3^-- and IO_3-containing ion clusters in coastal and polar environments, as well as complementary laboratory experiments in the absence of HO_x, have been interpreted as direct measurements of gas-phase iodic acid ($HOIO_2$, hereafter denoted as HIO_3) and HIO_3 clusters

(Sipilä et al., 2016) by ionization of the ambient species by NO_3^- in the instrument inlet. Since all possible reaction paths for I, IO, and OIO with H_2O are very endothermic (Canneaux et al., 2010; Hammaecher et al., 2011; Khanniche et al., 2017a) and $IO_x - H_2O$ complexes are very weakly bound (Galvez et al., 2013), the formation of oxyacids may rather proceed via hydrolysis of higher iodine oxides (Kumar et al., 2018):

$$I_2O_y + H_2O \rightarrow HIO_x + HIO_{y-x+1} \tag{R8}$$
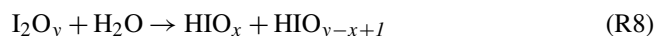
Ozone depletion and particle formation are to some extent competing processes. Significant I_xO_y photolysis rates may result in regeneration of IO_x:

$$I_2O_2 + hv \rightarrow IO + IO \tag{R9a}$$
$$\rightarrow I + OIO \tag{R9b}$$

$$I_2O_3 + hv \rightarrow IO + OIO \tag{R10a}$$
$$\rightarrow I + IO_3 \tag{R10b}$$

$$I_2O_4 + hv \rightarrow OIO + OIO \tag{R11a}$$
$$\rightarrow IO + IO_3 \tag{R11b}$$

These photochemical reactions would enhance ozone depletion while slowing down the incorporation of iodine into aerosol via oxides and/or oxyacids and represent an important source of uncertainty in the iodine chemical mechanism incorporated into global chemistry transport models (Saiz-Lopez et al., 2014; Sherwen et al., 2016). In order to reduce this uncertainty, we report here a set of I_xO_y photodepletion experiments with mass spectrometric detection, which enables unambiguous observation of all the species of interest (Gómez Martín et al., 2013). Experiments devoted to understanding the interaction between I_xO_y and water, potentially leading to the formation of HIO_3, are reported elsewhere (Gómez Martín et al., 2020).

2 Methods

2.1 Experimental set-up

A pulsed laser photolysis (PLP) system has been employed to generate iodine oxides from the photolysis of O_3 in the presence of I_2 in a tubular reaction cell (Fig. 1). A flow of typically 1.5 slm of He carrier gas (99.999 %, BOC Gases) was introduced in the reactor. I_2 molecules were entrained in the carrier flow by passing a smaller flow of He ($\sim$ 100 sccm) through a 12 mm diameter temperature-stabilized Teflon tube containing I_2 crystals (> 99.5 %, Sigma-Aldrich). An electrical discharge ozone generator converted $\sim$ 2 % of a $\sim$ 100 sccm O_2 flow (99.999 %, BOC Gases) to O_3, which was introduced to the main flow via an inlet on the flow tube.
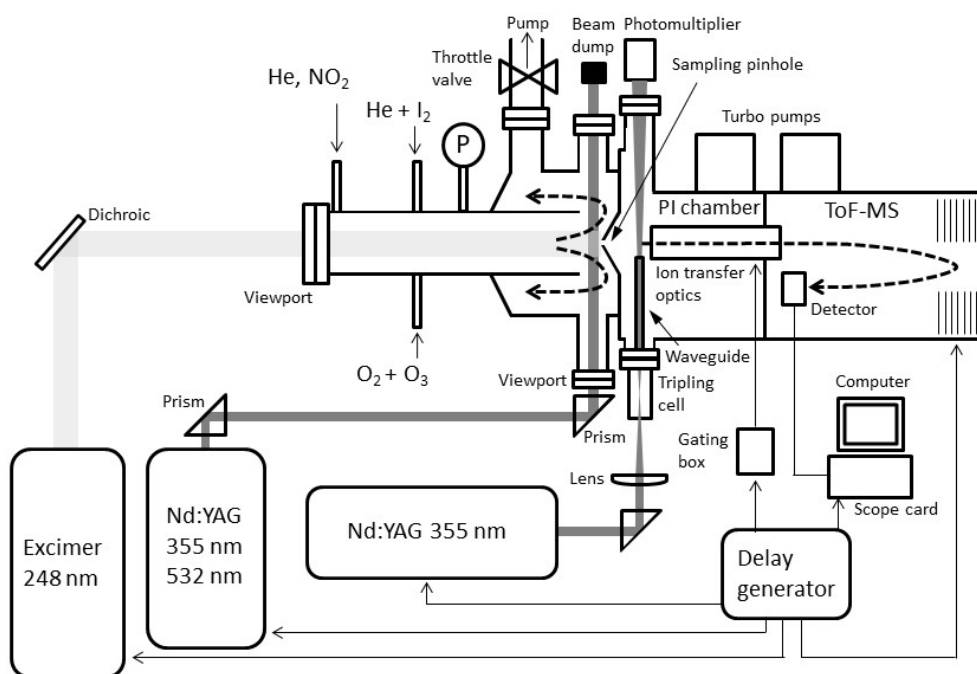
Figure 1. Schematic diagram of the experimental set-up for studying the photolysis of iodine oxides.

Ozone was photolysed at 248 nm by an excimer laser beam (Lambda Physik Compex 102), which was passed unfocussed through a quartz view port along the tube main axis. This generated the well-known sequence of reactions:

$$O_3 + h\nu \rightarrow O(^1D) + O_2 \tag{R12}$$

$$O(^1D) + M \rightarrow O(^3P) + M \tag{R13}$$

$$O(^3P) + I_2 \rightarrow IO + I \tag{R14}$$

This is followed by Reactions (R1), (R2), (R4), (R5), and (R6) as well as further I_xO_y clustering reactions. The precursor concentrations ($[I_2] \sim 2\text{–}4 \times 10^{14}$ molec. cm^{-3}, $[O_3] \sim 3\text{–}5 \times 10^{14}$ molec. cm^{-3}) and excimer laser energy (120–190 mJ pulse^{-1}, $\sim 50\text{–}80$ mJ pulse^{-1} cm^{-2}) were tuned to ensure that I_2 was in excess over $O(^3P)$. Iodine and ozone concentrations were measured using a 532 nm solid-state laser in a single-pass and multipass Herriott cell (Lewis et al., 2018), respectively (Fig. 2). A reflection (~ 5 %) of the main 532 nm diode laser (Thorlabs CPS532, 532 nm, 4.5 mW) beam was directed along the length of the cell (length $= 40$ cm) and detected using a photodiode detector (Thorlabs SM05PD3A). Ozone was detected by passing the main beam through a hole in the rear of a silver-coated concave mirror (Thorlabs CM508-200-P01, $f = 20$ cm) onto an identical mirror (without a hole) positioned 40 cm from the first mirror. The light was passed 40 times through the cell and exits through the same entrance hole (some passes are omitted from the diagram for simplicity), giving a path length of 12 m.

The concentrations C of O_3 and I_2 were then determined using the Beer–Lambert law (Eq. 1), where I and I_0 are the intensities of the 532 nm laser light recorded with and without the reagent present, respectively, OD is the optical density, σ the absorption cross section, and l the optical path length:

$$OD = \ln \frac{I_0}{I} = \sigma \cdot C \cdot l \tag{1}$$

O_3 has an absorption cross section at 532 nm of 2.34×10^{-21} cm^2 molec.$^{-1}$ (Burrows et al., 1999). A typical concentration of 5×10^{14} molec. cm^{-3} in the reaction mixture (total flow ~ 1700 sccm) requires a concentration in the O_3/O_2 flow (100 sccm) of around 8.5×10^{15} molec. cm^{-3}. An ozone concentration of 8.5×10^{15} molec. cm^{-3} results in OD $= 0.024$. I_2 has an absorption cross section at 532 nm of 3.03×10^{-18} cm^2 molec.$^{-1}$ (Saiz-Lopez et al., 2004). A typical I_2 concentration of 4×10^{14} molec. cm^{-3} in the reaction mixture (total flow ~ 1700 sccm) requires a concentration in the I_2/He flow (100 sccm) of around 6.8×10^{15} molec. cm^{-3}. An I_2 concentration of 6.8×10^{15} molec. cm^{-3} gives OD $= 0.82$. The ODs observed for both species are easily detectable by the instrument, which has a typical signal-to-noise ratio of ~ 400, which corresponds to a minimum detectable OD of 2.5×10^{-3}. As there is no reference photodiode in this setup, drift in laser intensity must be accounted for. To negate the effect of laser drift as much as possible, the probe intensity is measured over a period of 15 s for both I and I_0, with ~ 10 s between the measurements. To ensure that laser drift does not significantly affect the measured concentra-
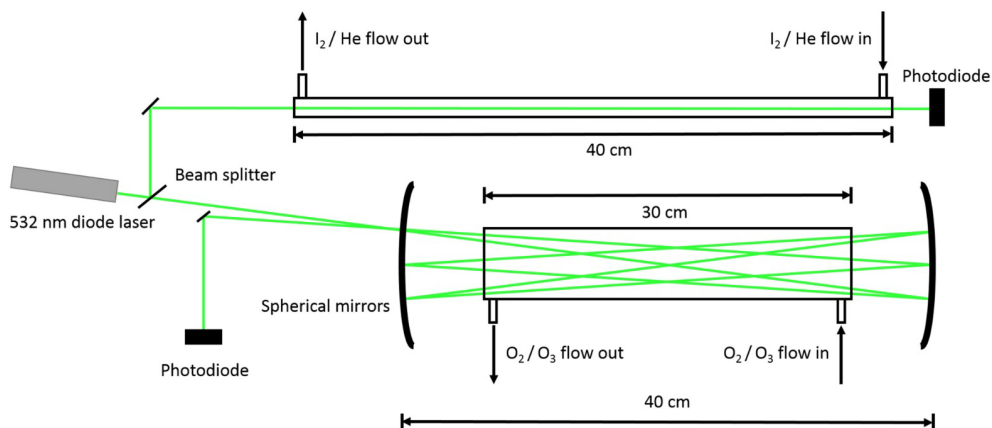
Figure 2. A schematic of the absorption set-up used to measure both I_2 and O_3.

tions, measurements are taken until three concordant results are obtained (typically the first three results).

In order to measure the photodepletion of the I_xO_y molecules at 532 and 355 nm, a frequency-doubled or frequency-tripled Nd:YAG laser beam (Continuum Surelite 10-II, $1\,cm^{-1}$ linewidth, 20 ns pulse width, $\sim$ $80\,mJ\,pulse^{-1}\,cm^{-2}$ at 532 nm, and $\sim 50\,mJ\,pulse^{-1}\,cm^{-2}$ at 355 nm) was passed across the flow tube, perpendicular to the main axis and near the sampling point. Experiments were carried out at 4–7 Torr. The pressure in the reactor was set by a throttle valve placed upstream of an Edwards 80 roots blower–oil rotary pump combination. The flows were set using calibrated MKS mass flow controllers and pressure was measured using a set of 10 and 1000 Torr MKS Baratron pressure transducers.

The iodine oxides generated were sampled in situ from the irradiated volume through a pinhole (200 μm diameter) situated on axis into a Kore Technology photo-ionization time-of-flight mass spectrometer (PI-ToF-MS) described in detail elsewhere (Gómez Martín et al., 2016). Successful detection of I_xO_y by this method has been demonstrated elsewhere (Gómez Martín et al., 2013; Wei et al., 2017; Gómez Martín et al., 2020). The PI chamber of this instrument ($\sim 10^{-4}$ Torr) is fitted with view ports, allowing a pulsed laser beam to be directed through the high-density region of the sampled gas jet. Iodine oxides have ionization potentials in the range of 9–11 eV (Gómez Martín et al., 2013; Wei et al., 2017), which requires generation of a vacuum ultraviolet (VUV) laser ionization beam. This is achieved by tightly focusing the 355 nm output of a frequency-tripled Nd:YAG laser (Continuum Surelite 10-II pulse width 3–5 ns) in a cell filled with xenon, which produces VUV radiation by frequency tripling (118 nm, or equivalently 10.5 eV) (Kung et al., 1973; Mahon et al., 1979). The resulting positive ions are accelerated towards the ToF-MS by means of a continuous negative voltage. An electron photomultiplier detector coupled to a pre-amplifier outputs an analogue signal, which
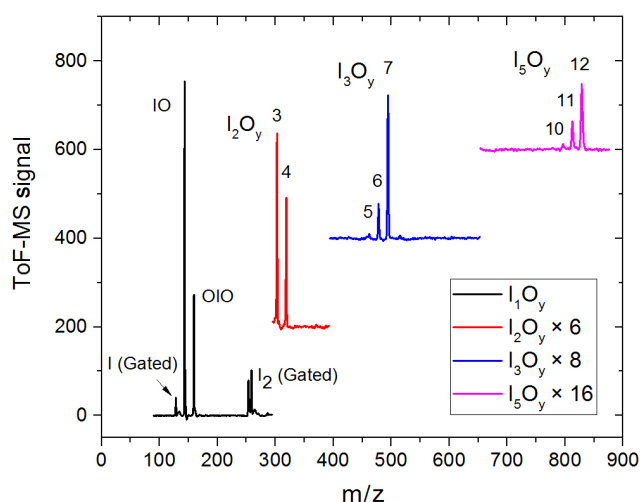

Figure 3. Mass spectra in four different m/z ranges encompassing peaks of species with one, two, three, and five iodine atoms. Some of the spectra are scaled and shifted for clarity. The mass spectra are generated by averaging the mass spectra at each time point over a 20 ms experiment comprising 20 individual time points.

is registered by the digital oscilloscope (Picoscope 6000). A limitation of this method is that large signals (e.g. I_2^+ and I^+) cause detector overload during a significant time span after the large peak has been registered. An analogue gating box is used to lessen these effects by sending a (~ 400 ns wide) gating pulse to the ion extraction optics. Gating in this way removed $> 90\,\%$ of the overloaded signal from I_2^+ and I^+, significantly improving the signal-to-overload ratio.

Synchronization between the chemistry-initiating excimer laser pulse, the photolysis laser, the probing PI laser pulse, and the detection devices is provided by a computer-controlled delay generator (Quantum Composers, 9518). In this manner, the delay between PLP and PI can be varied in order to observe the kinetics of reactants and products and the photodepletion of the species of interest. The experiment
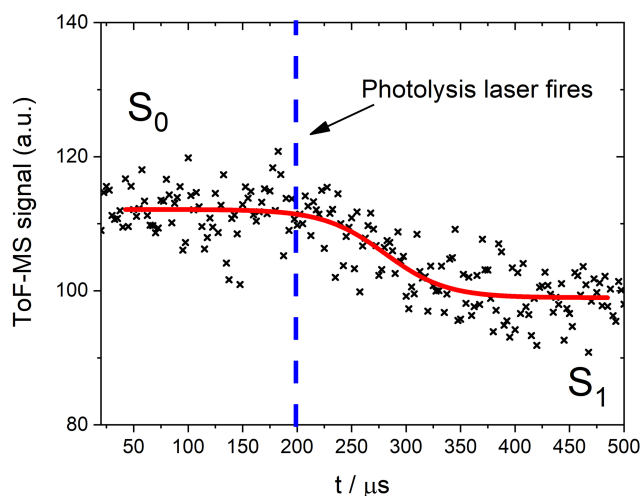
Figure 4. Schematic of a photodepletion measurement of NO_2. The red curve is an empirical fit through the data performed to obtain the values of S_0 and S_1.

repetition rate was set at 10 Hz, the optimal repetition rate for operation of both the VUV-generating PI YAG laser and the YAG laser used for photolysis of the iodine oxides. A LabView program built in-house provides a sequence of delays between the PLP and PI lasers which can be modified by the user via a graphical interface. Desired experimental parameters are input into the LabView program, including the number of pre-photolysis points, the number of experimental data, the duration of the experiment, and the number of repetitions. Each experiment results in a 3D dataset of signal intensity (proportional to concentration) vs. 248 nm photolysis–VUV photoionization delay time (kinetic profile or time trace) and time of flight (mass spectrum). Figure 3 shows mass spectra with the most prominent peaks obtained at different delay times. Mass-to-charge (m/z) calibration of time of flight was performed by selecting a number of well-known prominent mass peaks (e.g. IO at $m/z = 143$, OIO at $m/z = 159$, I_2O_3 at $m/z = 302$, I_2O_4 at $m/z = 318$, and I_3O_7 at $m/z = 493$ – Gómez Martín et al., 2013).

To investigate the photodepletion of I_xO_y, it is desirable to keep the signal of the species of interest relatively constant over the delay window used to probe the photolysis. The timing of the Nd:YAG photolysis laser pulse was programmed to a fixed delay with respect to the 248 nm excimer pulse. To find the optimal window in which to conduct photolysis experiments, the reaction kinetics were first explored between 0 and ~ 10 ms for different sets of conditions. It was important to generate a sufficiently high concentration of I_xO_y to obtain a good signal-to-noise ratio, but not so high that the growth/removal timescale was comparable to the observed photodepletion (~ 400 μs).

The trace shown in Fig. 4, which is similar to all the traces obtained in this experiment, exhibits a delay between the pre- and post-photodepleted signals. This delay corresponds to an instrumental sampling time depending on the alignment of the lasers and the molecular masses of the bath gas and the sample species (Baeza-Romero et al., 2012). In the present experiments, it was necessary to leave a small gap (~ 2 mm) between the photolysis volume and the sampling pinhole, so as to avoid hitting the skimmer cone with the laser. The diffusional exchange of molecules between the photodepleted volume and the un-photodepleted volume immediately before the pinhole blurs the onset of the photodepletion as it is measured by the ToF-MS. The values of S_0 and S_1 were obtained by empirically fitting the photodepletion trace to a sigmoidal function:

$$y = S_0 + \frac{S_1 - S_0}{1 + 10^{(\log x_0 - x)p}} \tag{2}$$

Fitting to this function ensures that the flat sections corresponding to the pre- and post-photodepletion concentrations (S_0 and S_1, respectively) are characterized in the precise regions outside of the aforementioned "blurred" zone. The parameters x and p are not of scientific importance for this study and are simply instrumental factors.

The photolysis laser depletes any analyte within the photolysis volume which exhibits a bound–unbound transition at the energy of the photolysis wavelength used for each experiment. The signals for a certain m/z ratio before and after the photolysis laser is fired are, respectively, noted as S_0 and S_1 (Fig. 4). Absorption cross sections were then calculated by comparing the relative signal change (ζ_{IxOy}) for the analyte of interest to the relative signal change (ζ_{REF}) for a molecule with a well-studied spectrum in an analogous actinometric experiment using the same configuration and laser fluence. In this way, systematic errors arising from the beam energy and area are eliminated in the determination of the actinic flux F:

$$\frac{S_{REF0} - S_{REF}}{S_{REF0}} = \frac{[X_{REF}]_0 - [X_{REF}]}{[X_{REF}]_0} \equiv \zeta_{REF}$$
$$= 1 - e^{-F \cdot \sigma_{X_{REF}} \cdot \phi_{X_{REF}}} \tag{3}$$

$$F = -\frac{1}{\sigma_{X_{REF}} \cdot \phi_{X_{REF}}} \ln(1 - \zeta_{REF}) \tag{4}$$

Similarly, for the target I_xO_y molecule we have the following:

$$\frac{S_{IxOy0} - S_{IxOy}}{S_{IxOy0}} = \frac{[I_xO_y]_0 - [I_xO_y]}{[I_xO_y]_0} \equiv \zeta_{I_xO_y}$$
$$= 1 - e^{-F \cdot \sigma_{I_xO_y} \cdot \phi_{I_xO_y}} \tag{5}$$

$$\sigma_{I_xO_y} \cdot \phi_{I_xO_y} = -\frac{1}{F} \ln(1 - \zeta_{I_xO_y}) \tag{6}$$

Inserting Eq. (4) into Eq. (6), we have the following:

$$\sigma_{I_xO_y} \cdot \phi_{I_xO_y} = \sigma_{X_{REF}} \phi_{X_{REF}} \frac{\ln(1 - \zeta_{I_xO_y})}{\ln(1 - \zeta_{REF})} \tag{7}$$

NO$_2$ (99.5 %, BDH, 10 % in He) was the best reference molecule to perform actinometry at 355 nm. In this case, $\sigma_{X_{REF}} = \sigma_{NO_2(355\,nm)} = 5.3 \times 10^{-19}$ cm^2 molec.$^{-1}$ (Vandaele et al., 1998) and $\phi_{X_{REF}} = \phi_{NO_2(355\,nm)} = 1$ (Burkholder et al., 2015). Typically, NO$_2$ depletion was around 8 % in the actinometric experiments. For the 532 nm photolysis experiments, OIO was chosen as the reference owing to the low sensitivity of its broad absorption bands to photolysis laser resolution, as opposed, for example, to I$_2$. The use of I$_2$ as an actinometer is also precluded by the overload issue mentioned above. The OIO absorption cross section at 532 nm is relatively well known, within 25 % of the average value of the four independent determinations reported in the literature (Bloss et al., 2001; Joseph et al., 2005; Spietz et al., 2005; Tucceri et al., 2006). On the other hand, conflicting results have been reported for the OIO photolysis quantum yield (Tucceri et al., 2006; Gómez Martín et al., 2009). Here we use the unit quantum yield reported by Gómez Martín et al. (2009), which was determined in a system free of interferences from ozone where a long-lived I atom photofragment and no reformation of OIO were observed over a timescale of several milliseconds. This result is also supported by the short lifetime (200 fs) of the excited state responsible for the observed absorption bands (Ashworth et al., 2002) and the existence of a feasible photolysis path revealed by high-level ab initio calculations (Peterson, 2010). Thus $\sigma_{X_{REF}} = \sigma_{OIO(532\,nm)} = 9.5 \times 10^{-18}$ cm^2 molec.$^{-1}$ (Bloss et al., 2001; Spietz et al., 2005) and $\phi_{X_{REF}} = \phi_{OIO(532\,nm)} = 1$ (Gómez Martín et al., 2009). In principle, Eq. (7) yields the photolysis cross section, i.e. the product $\sigma_{I_xO_y} \cdot \phi_{I_xO_y}$, which is equal to the absorption cross section if $\phi_{I_xO_y} = 1$. This is a reasonable assumption for broadband absorption spectra, indicating excitation to an unbound upper state. The photolysis processes in this study therefore do not depend on the nature and pressure of the carrier gas matrix, and the results can be applied directly in atmospheric models.

2.2 Ab initio calculations

The geometry of the ground electronic state of IO$_3$, I$_2$O$_3$, I$_2$O$_4$, I$_3$O$_6$, and I$_3$O$_7$ was optimized by using the B3LYP functional combined with the standard 6-311+G(2d,p) triple-ζ basis set for O and H and an all-electron (AE) basis set for I (Glukhovtsev et al., 1995). The AE basis set is a contracted (15s12p6d)/[10s9p4d] 6-311G basis, the [5211111111, 411111111, 3111] contraction scheme supplemented by diffuse s and p functions, together with d and f polarization functions. See Glukhovtsev et al. (1995) for further details. Figure A1 illustrates the geometries of the various iodine oxides and hydroxy species that are discussed in Sect. 4. The corresponding molecular parameters (Cartesian coordinates, rotational constants, and vibrational frequencies) are listed in Appendix Table A1. Note that the ground states of some of these oxides have been studied at

a higher level of theory elsewhere (Kaltsoyannis and Plane, 2008; Galvez et al., 2013).

The absorption cross sections of the aforementioned molecules were calculated using the time-dependent density functional (TD-DFT) excited states method (Stratmann et al., 1998) within the Gaussian 16 suite of programs (Frisch et al., 2016). The vertical excitation frequencies ($\tilde{v}_i$) and oscillator strengths (f_i) were obtained for the first 30 excited states (Table A2–A4). The cross section $\sigma(\tilde{v})$ at frequency $\tilde{v}$ was then computed using the GaussView program (Dennington et al., 2016):

$$\sigma(\tilde{v}) = 2.17 \times 10^{-16} \sum_{i=1}^{n} \left(\frac{f_i}{\Delta} \exp\left[-\left(\frac{\tilde{v} - \tilde{v}_i}{\Delta} \right)^2 \right] \right) \quad (8)$$

The summation is over the 30 electronic excited states and $\sigma(\tilde{v})$ is in units of cm^2 molec.$^{-1}$. Each peak is assumed to have a Gaussian band shape with a width Δ, set here to the default value (Dennington et al., 2016) of 0.4 eV. Although there are more advanced methods for the calculation of electronic spectra, TD-DFT offers a reasonable compromise between low computational cost and accuracy of the predicted transitions. Figure A2 shows a comparison between the experimental and TD-DFT absorption spectra of IO, OIO, and HOI. Note that although the TD-DFT method is not designed to predict ro-vibrational structure, the spectral positions of the electronic bands and the average absorption cross sections are in reasonable agreement with the experiment, even in the case of open-shell species like IO and OIO. Higher iodine oxides are closed-shell molecules and the accuracy of the transitions is expected to be similar to the result for HOI.

2.3 Photolysis rate calculations

In this study we employ the CAM-Chem (Community Atmospheric Model with Chemistry, version 4.0) global 3D model, included in the CESM framework (Community Earth System Model) (Lamarque et al., 2012), to estimate the photolysis rate (J) of the different I$_x$O$_y$ species according to their computed absorption cross section, constrained by the experimental data at 532 and 355 nm. CAM-Chem has been configured with a 2.5° longitude by 1.9° latitude spatial resolution and 26 vertical levels (from the surface to up to 40 km). The model was run in the specified dynamics mode (Lamarque et al., 2012), using offline meteorological fields from a previous free-running climatic simulation (Fernandez et al., 2014; Saiz-Lopez et al., 2015).

CAM-Chem implements a state-of-the-art halogen chemistry scheme (Fernandez et al., 2014; Saiz-Lopez et al., 2014; Saiz-Lopez et al., 2015). This chemical scheme is fed by both organic and inorganic halogen emission sources (Ordóñez et al., 2012; MacDonald et al., 2014). Saiz-Lopez and co-workers (Saiz-Lopez et al., 2014, hereafter SL2014) conducted two sets of simulations without and with the photolysis of I$_x$O$_y$ oxides in CAM-Chem to evaluate the range of

inorganic iodine loading, partitioning, and impact in the troposphere. The photolysis of I_xO_y was based on the best available knowledge at that time on the major I_xO_y species (I_2O_2, I_2O_3, and I_2O_4) and their absorption cross sections (Gómez Martín et al., 2005; Gómez Martín et al., 2013). In this study we run photolysis simulations and compare the J values with the new cross sections to those in SL2014.

3 Results

3.1 Photolysis at 355 nm

As described in the experimental section, kinetic profiles of the growth and removal of the target iodine oxide species shown in Fig. 3 were carried out in order to define the time periods with the most suitable kinetic profiles for photolysis measurements (Fig. 5). Fragmentation of iodine oxides was a significant problem in these experiments, as predicted from ionization energy calculations of larger iodine oxides to possible photofragments at 10.5 eV (Gómez Martín et al., 2020). High amounts of active iodine ($IO_x=I$, IO) released from Reaction (R12) lead to fast formation of I_xO_y and particles. Under these conditions, at long times after the peak IO and OIO ($\sim$ 3–5 ms), the observed signal of IO, OIO, and I_xO_y is contaminated by photofragmentation of higher-order iodine oxides. For this reason, great care needed to be taken to establish a time window for each species wherein higher oxides are not present, to ensure that any depletion in the mass spectrometric signal for each species is exclusively due to the removal of the species via photolysis (Fig. B1). Evidence of fragmentation comes in the form of a secondary growth in the signal seen for IO and OIO (Fig. 5). The delay between the excimer and the Nd:YAG photolysis laser was therefore carefully selected to coincide with a period of relatively constant signal of the desired analyte, typically a maximum for short-lived species, or a slow rise for larger reaction products of interest.

In the case of IO and OIO, the photolysis delay was selected based on the location of the maxima of their kinetic profiles. Typically, this was around 1 and 2 ms for IO and OIO, respectively. IO showed a clear depletion of $\sim$ 20 % at 355 nm (Fig. 6a) corresponding to a cross section of $\sigma_{355\,nm,\,IO} = (1.2 \pm 0.1) \times 10^{-18}\,cm^2\,molec.^{-1}$ (based on an average of three measurements), in excellent agreement with the most recent determinations based on absorption spectroscopy (Bloss et al., 2001; Spietz et al., 2005), where the presence of an underlying absorption corresponding to a product of Reactions (R2), (R4), (R5), or (R6) was accounted for (Atkinson et al., 2007) (Fig. 6b). We consider the mutual consistency between our measurement and the most reliable determinations of the IO cross section at 355 nm to be a validation of our method for determining the absorption cross sections of I_xO_y species.
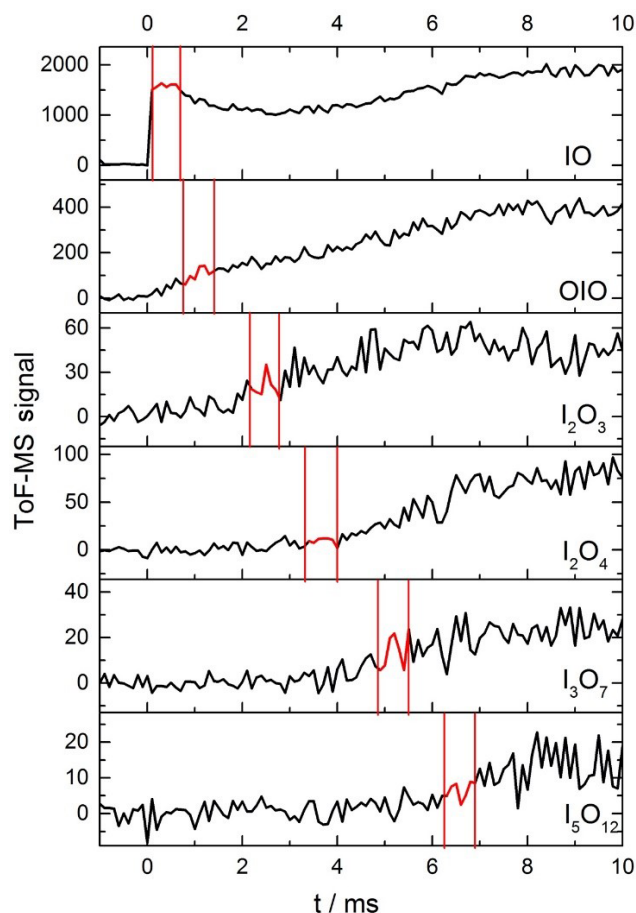

Figure 5. Time traces of IO, OIO, I_2O_3, I_2O_4, I_3O_7, and I_5O_{12} from -1 to 10 ms, at 1 ms intervals for a mixture of He (10 torr), O_3, and I_2 ($[O_3] = 4 \times 10^{14}\,molec.\,cm^{-2}$ $[I_2] = 2.8 \times 10^{14}\,molec.\,cm^{-2}$) flash photolysed by an excimer pulse at $t = 0$ (130 mJ pulse^{-1}). The red sections highlighted for each species correspond to the optimal delay windows for photolysis of the corresponding species for this set of conditions.

As expected, no significant depletion was observed for OIO, with an upper limit of $\sigma_{355\,nm,OIO} < 10^{-19}\,cm^2\,molec.^{-1}$ based on the noise of the mass spectrometric signal at m/z 159. No significant depletion was observed for I_2O_3 ($m/z = 302$) at 355 nm (Fig. 7, top left), and an upper limit for the absorption cross section of $\sigma_{355\,nm,I2O3} < 5 \times 10^{-20}\,cm^2\,molec.^{-1}$ was determined based on the average noise of the I_2O_3 signal. By contrast, I_2O_4 was depleted by 355 nm photolysis by $\sim$ 40 % (Fig. 7, top right), corresponding to a photolysis cross section of $\sigma_{355\,nm,\,I2O4} = (2.7 \pm 0.3) \times 10^{-18}\,cm^2\,molec.^{-1}$ (based on an average of two measurements). The determined cross sections and upper limits at 355 nm are listed in Table 1.

Fragmentation precludes determination of photolysis products at 355 nm (channels of photochemical Reactions R9–R11) due to the fact that the signal arising from
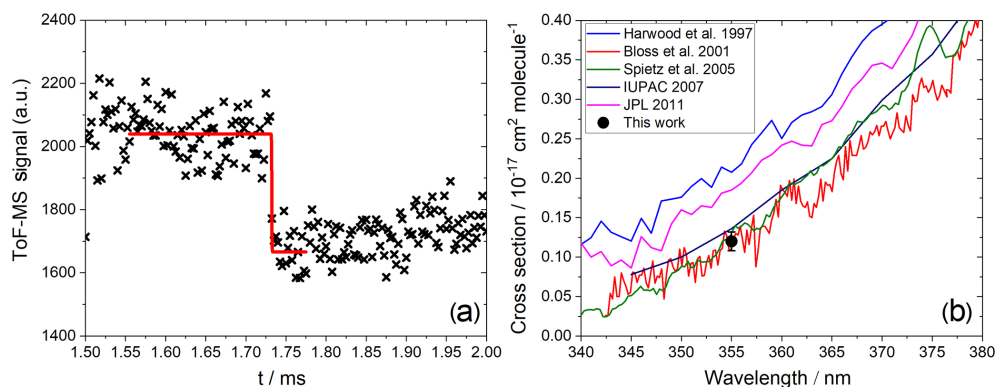
Figure 6. (a) Measured photodepletion of IO ($m/z = 143$). **(b)** Comparison of a published absorption cross section with the absorption cross section at 355 nm determined in this work.
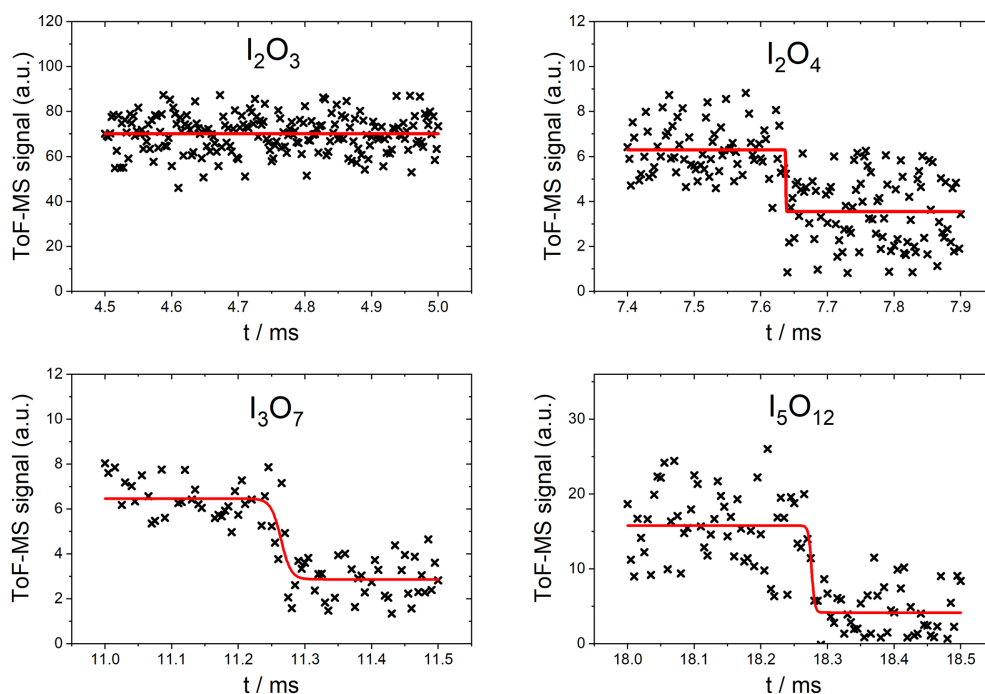

Figure 7. Measured photodepletion at 355 nm of I_2O_3, I_2O_4, I_3O_7, and I_5O_{12}. The laser was triggered at 4.75 ms in the I_2O_3 experiment. The red line indicates the fit to Eq. (2).

precursor ions (which may be 355 nm photolysis products) is indistinguishable from product ions resulting from fragmentation of higher oxides due to the 118 nm photoionization. For any given species, possible increases in signals corresponding to products of photolysis at 355 nm are offset by the decrease in the precursor ion concentration and therefore the product ion signal. As an example, consider I_3O_7 photolysis at 355 nm. The peaks of the possible photolysis products I_2O_3, I_2O_4, OIO, and IO (referred to here as photofragments) prior to photolysis will have contributions from the precursor ion signals of these species as well as product ion signals of I_3O_y. Upon photolysis of I_3O_7, the concentration of I_3O_7 will decrease, causing a decrease in the precursor ion

signal and therefore the product ion signals, resulting in turn in a net negative impact on the amplitude of all product ion signals. In addition to the decrease in product ion signals resulting from possible photofragment species, the precursor ion signal for the photolabile species (IO, I_2O_4 in this example) will decrease due to direct photolysis of these species. Concurrently with the decrease in the I_3O_7 precursor ion signal, there will be a positive contribution to some or all of the concentrations of possible photofragment precursor ion signals. It is impossible to separate these contributions to the net change in signal magnitude, and therefore the products of these photolysis processes cannot be determined.
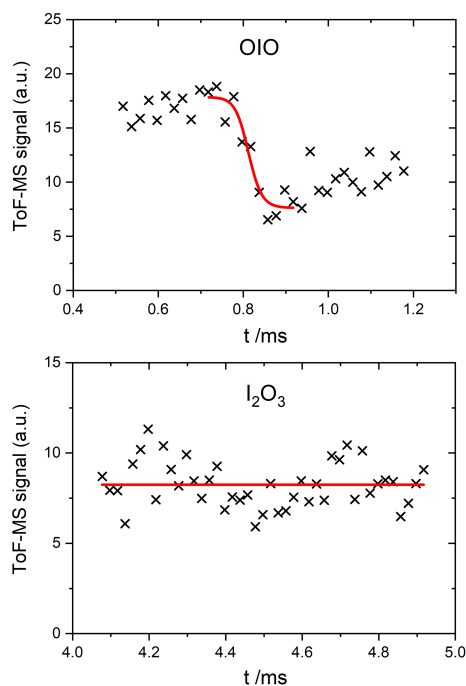
Figure 8. Measured photodepletion at 532 nm of OIO and I_2O_3. The laser was triggered at 4.5 ms in the I_2O_3 experiment.

Table 1. Absorption cross sections of iodine oxides at 532 and 355 nm.

Species	$\sigma_{355\,nm}$/cm^2 molec.$^{-1}$	$\sigma_{532\,nm}$/cm^2 molec.$^{-1}$
IO	$(1.2 \pm 0.1) \times 10^{-18}$	a
OIO	$< 10^{-19}$	b
I_2O_3	$< 5 \times 10^{-19}$	$< 5.0 \times 10^{-19}$
I_2O_4	$(3.9 \pm 1.2) \times 10^{-18}$	$< 1.3 \times 10^{-18}$
I_3O_6	$(6.1 \pm 1.6) \times 10^{-18}$	$< 1.5 \times 10^{-18}$
I_3O_7	$(5.3 \pm 1.4) \times 10^{-18}$	$< 1.4 \times 10^{-18}$
I_5O_{12}	$(9.8 \pm 1.0) \times 10^{-18}$	$< 1.5 \times 10^{-18}$

[a] The $0 \leftarrow 0$ band of IO is placed at 465.5 nm (Spietz et al., 2005), and therefore, there cannot be any band of ground state IO ($v'' = 0$) at a longer wavelength. There is a hot band at ~ 530 nm ($0 \leftarrow 4$), but the $v'' = 4$ state is not populated at room temperature in equilibrium. [b] Actinometer.

constant energy shift means assuming that all the excited state energies are offset by a constant amount with respect to the ground state.

4 Discussion

4.1 Absorption spectra

A time-dependent broadband absorption was observed by Bloss et al. (2001) concurrently with the IO self-reaction decay, which was assigned to I_2O_2. The shape of the band was observed to be different for $\lambda < 360$ nm depending on the chemical scheme employed to generate iodine oxides. Later, a broadband absorption with a similar spectral slope was reported (Fig. 9) together with targeted UV measurements showing that the band peaks around 250 nm (Gómez Martín et al., 2005; Spietz et al., 2005). The kinetics of the absorption spectrum for $\lambda > 310$ nm were found to result from the overlap of at least two different species, one dominating the absorption below 340 nm (labelled Y) and another one dominating from 340 nm towards the visible (labelled Z). It was found that the kinetics of species Y was compatible with a product of the IO self-reaction, i.e. I_2O_2. By contrast, Z, which would be similar to the spectrum measured by Bloss et al. for $\lambda > 360$ nm, was not compatible with a product of the IO self-reaction, and it was tentatively assigned to I_2O_3.

Gómez Martín et al. (2005) derived the cross section of the species Y and Z at 322 and 356 nm, respectively, using an iodine mass conservation approach where the depletion of the I_2 precursor was balanced by the sum of atomic iodine contained in the oxides formed after the photolysis pulse. The cross sections were determined on a per iodine atom basis. Assuming absorbers with two iodine atoms, the spectra of Y and Z were scaled as shown in Fig. 9 (Saiz-Lopez et al., 2014). Since the spectra are featureless, they can be assumed to result from bound to free transitions, justifying a unit photolysis quantum yield of the molecules generating them.

As indicated by Reactions (R10b) and (R11b), IO_3 ($m/z = 175$) is a potential product of I_2O_3 and I_2O_4 photolysis. However, this species has never been observed in the gas phase. According to our ab initio calculations, the ionization potential of IO_3 is 12.1 eV, which is higher than the photoionization energy employed in the present work (10.5 eV).

3.2 Photolysis at 532 nm

As expected (Gómez Martín et al., 2009), OIO shows strong depletion in the 532 nm photolysis experiments (Fig. 8), and it is therefore used as the actinometer at this wavelength. None of the higher-order iodine oxides showed measurable depletion above the noise (as an example the I_2O_3 trace is shown in Fig. 8). Table 2 lists the upper limits to the absorption cross sections of each species at 532 nm, determined from the signal-to-noise ratio of the recorded traces.

3.3 Ab initio spectra

The calculated spectra are displayed in Fig. 9 (I_2O_2, I_2O_3, and I_2O_4), Fig. 10 (I_3O_6 and I_3O_7), and Fig. 11 (IO$_3$). Oscillator strengths of the electronic transitions that are responsible for the visible and UV absorptions are provided in Appendix A. The TD-DFT spectra were wavelength-shifted by applying a constant energy shift to get agreement with the experiment at 355 nm. The shifts are quite modest, within the expected error at this level of theory (Foresman and Frisch, 2015): I_2O_3 (30 kJ mol^{-1}), I_2O_4 (-12 kJ mol^{-1}), I_3O_6 (9.2 kJ mol^{-1}), and I_3O_7 (-21 kJ mol^{-1}). Applying a
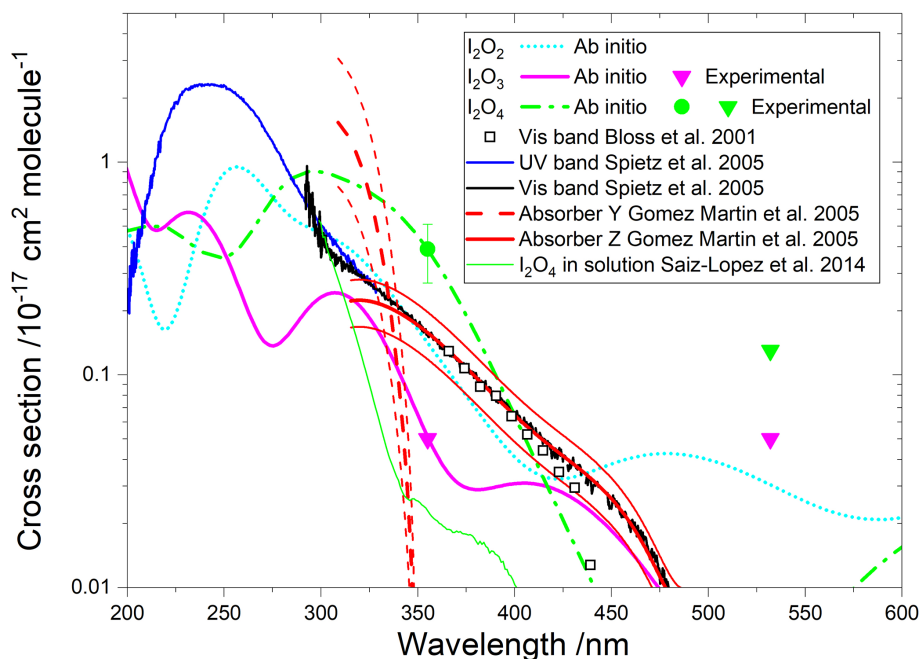
Figure 9. Absorption cross sections of I_2O_2, I_2O_3, and I_2O_4. The cyan, pink, and green lines correspond to the respective ab initio spectra. The pink and green symbols indicate, respectively, the measured absorption cross sections of I_2O_3 and I_2O_4 (triangles indicate upper limits). The empty squares correspond to an absorption band reported by Bloss et al. (2001) in 8 nm interval averages for $\lambda > 362$ nm. The blue and black lines correspond to absorption bands reported by Spietz et al. (2005). The latter was found to be a superposition of two absorptions with different kinetic behaviour, denoted Y (dashed red line) and Z (solid red line) (Gómez Martín et al., 2005). The thin red lines represent the uncertainties of these spectra, which mainly originate from the absolute absorption cross sections of Y and Z at 322 and 356 nm, respectively. A spectrum of I_2O_4 in solution is indicated in green (Saiz-Lopez et al., 2014).
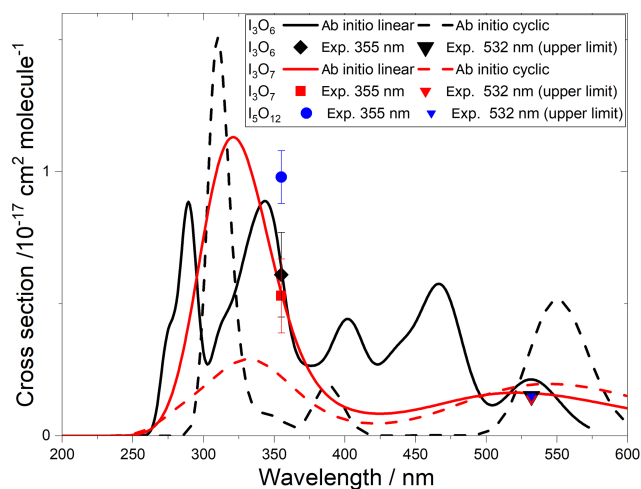

Figure 10. Absorption cross-section spectra of I_3O_6 (black lines and symbols), I_3O_7 (red lines and symbols), and I_5O_{12} (blue symbols). Ab initio spectra of linear and cyclic isomers are shown by solid and dashed lines, respectively.

The absorption cross sections determined in this work from photodepletion of I_2O_3 and I_2O_4 at 355 nm do not confirm the previous tentative assignment of absorber Z to I_2O_3. The cross section of I_2O_4 obtained from our photodepletion experiments is in better agreement with the absorber Z. Also, it appears that the spectrum of I_2O_4 in solution largely underestimates the gas-phase spectrum. The absorption of Z at 355 nm in Fig. 9 lies slightly below the I_2O_4 cross section determined in the present work, which is consistent with a contribution to Z of other I_xO_y species with $x>2$ (i.e. the scaling of the spectrum should be effectively higher than the factor of 2 used by Gómez Martín et al., 2005). In fact, the theoretical spectra of I_2O_4, I_3O_6, and I_3O_7 (Figs. 9 and 10) show similar shapes between 300 and 500 nm. It is very likely that the absorption band extending from 200 nm to nearly 500 nm (blue and black lines in Fig. 9) results from the overlap of absorptions corresponding to several I_xO_y species. Therefore, these experimental absorption spectra are not useful for photolysis rate calculations unless further deconvolution enables separation of the different contributions.

The calculated spectra shown in Figs. 9 and 10 agree generally well with the experimentally determined values at 355 and 532 nm after small wavelength shifts indicated above. As shown in Fig. 10, the upper limits from experiment are within 20 % of the theoretical calculations for linear I_3O_6
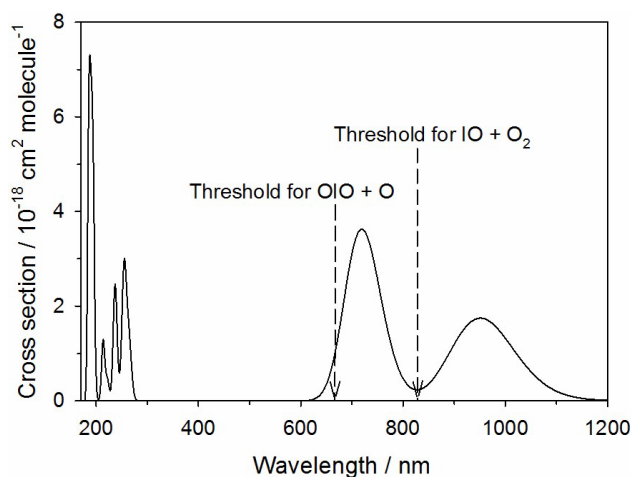
Figure 11. Absorption spectrum of IO_3 calculated at the TD/B3LYP/gen level of theory (see text for further details). The arrows indicate the energy thresholds for the two photodissociation pathways.

Figure 12. Potential energy surface for the reaction between IO_3 and HO_2 to produce HIO_3, calculated at the B3LYP/gen level of theory (see text for further details).

and I_3O_7. Note that theoretical absorption cross-section spectra for both the linear and cyclic forms (Fig. 5) of I_3O_6 and I_3O_7 are shown in Fig. 10. The linear forms of both species fit significantly better to the experimental values, suggesting the linear form is the one which is formed preferentially in these reactions.

4.2 Photolysis products

The likely photodissociation pathways of I_2O_3 and I_2O_4 can be elucidated by seeing how the geometry of each excited state relaxes after vertical excitation from the ground-state geometry using the TD-DFT method (see Sect. 2.2). In the case of I_2O_3, excitation in both the bands at 334 and 453 nm (Fig. 9) produces a pronounced extension of the I–IO_3 bond, indicating photolysis leading to I + IO_3 (Reaction R10b). For I_2O_4, excitation at 667 nm and in its strong band at 324 nm produces IO + IO_3, whereas absorption in the weak band at 366 nm produces OIO + OIO.

The theoretical absorption spectrum of IO_3 is shown in Fig. 11, calculated at the same level of theory as described in Sect. 2.2. IO_3 absorbs in the tropospheric solar actinic range in two near-IR bands centered at 710 and 950 nm. There are two possible photolysis pathways:

$$IO_3 + h\nu \rightarrow OIO + O \tag{R15a}$$
$$\rightarrow IO + O_2 \tag{R15b}$$

The first channel requires $180\,kJ\,mol^{-1}$ to break the O_2I–O bond (not including spin-orbit coupling), corresponding to a photolytic threshold of 665 nm. Reaction (R15b) is closely analogous to the photolysis of OIO in its band between 500 and 600 nm, where the I atom is squeezed out from between the two O atoms in a process that overall is actually
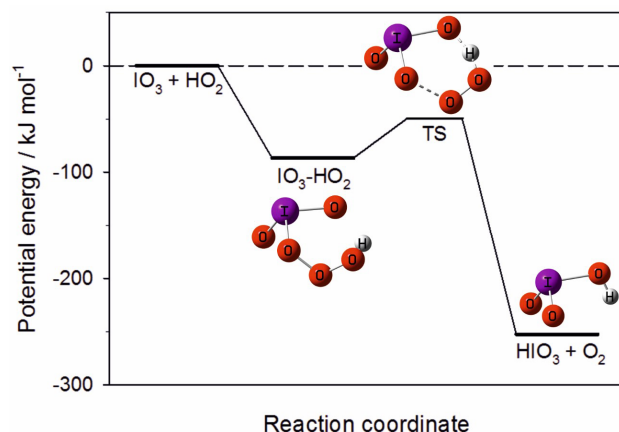
exothermic because of the strength of the newly formed O_2 bond (Gómez Martín et al., 2009). In the same way, Reaction (R15b) is exothermic by $78\,kJ\,mol^{-1}$. However, there is a barrier of $145\,kJ\,mol^{-1}$ involved in squeezing the IO out from between the two oxygen atoms. This corresponds to a photolytic threshold of 827 nm. Both of these thresholds are indicated in Fig. 11. This shows that absorption across the entire 710 nm band is sufficient for photolysis via Reaction (R15b) to occur. If that were the case, then $J(IO_3 \rightarrow IO + O_2)$ could be as large as $0.15\,s^{-1}$. Photolysis via Reaction (R15a) is just possible in the short wavelength tail of the 710 nm band, so $J(IO_3 \rightarrow OIO + O)$ could be as large as $0.007\,s^{-1}$. It therefore seems likely that photolysis of IO_3 is fast and mainly produces IO.

If, however, photolysis of IO_3 is significantly slower than this upper limit, the molecule could persist in the atmosphere long enough to undergo reaction with other molecules. An intriguing possibility is that IO_3 may be a source of HIO_3. The reaction

$$IO_3 + H_2O \rightarrow HIO_3 + OH \tag{R16}$$
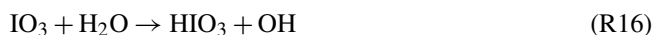
is endothermic by $25\,kJ\,mol^{-1}$ ($14\,kJ\,mol^{-1}$ according to previous work at a higher level of theory; Khanniche et al., 2017b) and so most likely does not occur. However, the reaction

$$IO_3 + HO_2 \rightarrow HIO_3 + O_2 \tag{R17}$$

is very exothermic, with a deep submerged barrier (Fig. 12). A Rice–Ramsperger–Kassel–Markus (RRKM) calculation using the MESMER program (Glowacki et al., 2012) with the molecular parameters in Table 1 indicates that the rate constant of Reaction (R17) is k (290 K) $\sim 3 \times 10^{-11}\,cm^3\,molec.^{-1}\,s^{-1}$. Given that $[HO_2]$ is typically $3 \times 10^8\,molec.\,cm^{-3}$ at midday (Stone et al., 2012), IO_3 could be converted to HIO_3 with a reaction rate of $\sim 0.01\,s^{-1}$, i.e.

about 15 times slower than the upper limit to the photolysis rate discussed above. Reaction (R17) could therefore provide a route to HIO_3 formation, and this should be the subject of future investigation.

4.3   Atmospheric implications

The theoretical spectra constrained with the measurements at 355 and 532 nm have been implemented in CAM-Chem in order to calculate photolysis rates for I_2O_y ($y = 2, 3, 4$) and I_3O_7. Having anchored the theoretical absorption spectra at 355 nm, we then assume that photolysis is possible up to the dissociation limit (which is the case for all the transitions of the I_xO_y ($x > 1$) molecules). A conservative estimate is a factor of 2 uncertainty in the J values for these molecules. The main changes with respect to SL2014 are the following:

i.   The new I_2O_2 cross sections are lower in the UV than those of the absorber Y used in SL2014 (Fig. 9) and extend over a wider range of the actinic range.

ii. I_2O_3 and I_2O_4 have, respectively, lower and higher absorption cross sections than in SL2014 as a result of replacing the absorption Z and the I_2O_4 spectrum in solution in favour of theoretical spectra constrained with experimental values. The cross section of I_2O_3 is lower, but only by a factor of ~ 2 in the important region between 350 and 450 nm. The cross sections of I_2O_4 increase by 1 order of magnitude with respect to the spectrum in solution.

iii. Higher iodine oxides like I_3O_7 and I_5O_{12} not included in SL2014 also photolyse. They show bands in the green part of the spectrum (Fig. 10) and therefore have higher photolysis rates than I_2O_4.

Annual zonal-average photolysis rate plots are shown in Figs. 13 and 14. Surface atmospheric photolysis of all the I_xO_y species is generally fastest between 30 and $-30°$ latitude, displaying slight minima at 5 and $-5°$ latitude due to attenuation of actinic flux by cloud cover at the intertropical convergence zone. Average I_xO_y global J values in the upper troposphere exhibit a maximum around $5°$ latitude, where solar flux is highest. At $5°$ latitude, I_2O_2 and I_2O_4 J values are largest at an altitude of 8 km. Similarly, the J values for I_2O_3 and I_3O_7 at $5°$ latitude are highest at 8 km and then remain relatively constant above 20 km. In contrast with J values for I_xO_y at $5°$ latitude, values at mid latitudes increase with altitude, showing no maxima at 8 km. The observed increase in J values at 8 km is explained by the albedo effect of cloud cover in certain regions, particularly the intertropical convergence zone, contributing to the total (incident + reflected) solar flux in these regions.

Figure 13d–f show the percentage difference between the SL2014 J values and those calculated in this study. As a result of the new I_2O_2 cross sections extending across the actinic window, this species shows an increase in J values

at all latitudes, with the largest increases seen at the poles ($\sim 300\%$ increase) and lower increases of around 100% near the Equator. I_2O_3 shows a uniform decrease of around 46% across all latitudes and altitudes, as expected from the approximately uniform decrease in the new spectrum with respect to absorber Z, which was taken as I_2O_3 in SL2014. I_2O_4 exhibits the largest increase in J values across all latitudes, ranging from 750% at 40 km between -30 and $30°$ latitude up to increases above 1000% at the poles. Photolytic lifetimes of I_xO_y species in the troposphere vary from a few seconds for the most photolabile species, i.e. I_3O_7, to several minutes for I_2O_3, which has the smallest absorption cross sections in the actinic region and the smallest J values of the species in this study. Mid and high latitudes exhibit particularly low J surface values and encompass many coastal regions where active iodine concentrations are high and iodine-driven particle formation has been reported (Saiz-Lopez et al., 2012b).

Photolysis of higher iodine oxides (Reactions R9–R11) competes with gas-to-particle formation (R7) and recycles IO_x, which participates in ozone-depleting cycles (e.g. R1–R3). Therefore, higher J values at the surface tend to hinder particle formation and enhance ozone depletion. The new spectra result in decreased photolysis lifetimes of I_2O_2 (factor of ~ 3) and I_2O_4 (factor of ~ 10) and indicate that photolysis of nascent iodine clusters such as I_3O_7 and I_5O_{12} may further slow down particle formation. On the other hand, the lifetime of I_2O_3 is approximately doubled, which increases the chances of participating in other reactions, including clustering with other I_xO_y. Whether this may balance the decrease in the photolysis lifetimes of other species or not remains to be studied in future work. I_2O_3 is believed to be an important iodine reservoir and key intermediate in the formation of new particles (Gómez Martín et al., 2013; Saiz-Lopez et al., 2014), but there is a substantial lack of mechanistic information about iodine oxides and how they may convert (or not) into HIO_3.

Another active iodine chemistry region is the tropical upper troposphere–lower stratosphere region (UTLS), where significant concentrations of iodine exist (Koenig et al., 2020) as a result of strong convection carrying iodine precursors emitted at the ocean surface (mainly CH_3I). The effect of the new spectra on the J values in this region is similar to the effect at the surface, although the changes are less pronounced. In the UTLS, I_xO_y molecules play the role of iodine reservoirs and, as a result of the enhanced actinic flux (see J maxima between 8 and 17 km around the Equator in Figs. 12 and 13), their photolysis has a significant impact on ozone depletion in this climatically sensitive region (Saiz-Lopez et al., 2012a). Iodine recycling in aerosol is believed to play an important role in explaining observed concentrations of gas-phase IO_x (Koenig et al., 2020). The form in which gas-phase iodine (oxides, oxyacids, or nitrate) is taken up in sulfate aerosol may also determine the extent to which iodine can return to the gas phase.
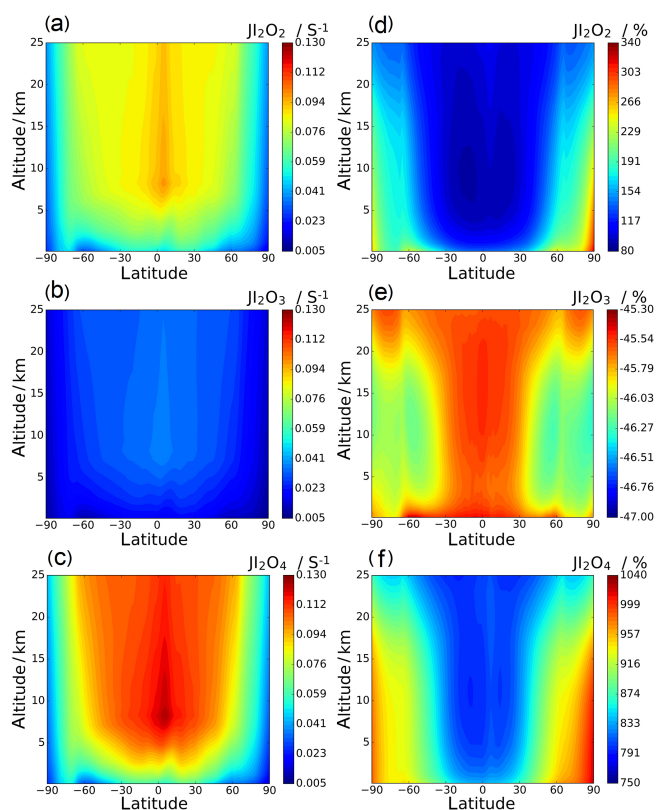
Figure 13. Annual zonal-average J value vertical profiles for I_2O_2, I_2O_3, and I_2O_4 (**a**, **b**, and **c**, respectively; note that the colour scale is the same for these three panels) and the percentage change between the SL2014 annual zonal-average J value vertical profiles and the profiles in this study (**d**, **e**, and **f**, respectively).

To investigate with more detail the effect of the new spectra on particle formation, iodine speciation in aerosol, and ozone depletion, the iodine chemistry scheme in CAM-Chem needs to be expanded to include the photolysis products and yields of I_xO_y photolysis reactions as well as the reactions of the possible photoproducts, which are poorly known. New laboratory and theoretical work is required to solve these uncertainties. The mechanism of iodine oxide particle (IOP) formation remains controversial, with two possible pathways proposed via I_xO_y and HIO_3. Work on the IOP formation mechanism conducted in the course of this research has been published elsewhere (Gómez Martín et al., 2020). Future laboratory measurements of I_xO_y spectra and kinetics may benefit from a multiplexed approach where tuneable photoionization mass spectrometry, absorption spectroscopy, and multi-wavelength laser photodepletion are used concurrently. A follow-up modelling study will be conducted with an updated mechanism for atmospheric iodine chemistry, including the photochemistry outlined in this paper, as well as a chemical scheme for IOP formation.
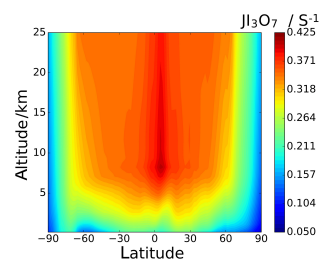

Figure 14. Annual zonal-average vertical J value profile for I_3O_7 (not included in SL2014).

5 Conclusion

The photodepletion laboratory experiments reported in this work confirm that I_xO_y species are photolabile, and therefore this work supports the $J(I_xO_y)$ scenario in ASL2014, with important consequences for ozone depletion. The values of the absorption cross sections obtained at 355 and 532 nm have been employed to revisit the assignment of absorption bands in previous work. Also, comparison between theoretical spectra and measurements gives some clues about the geometry of the molecules. I_2O_3 has a smaller absorption cross section in the actinic region than previously thought, which may facilitate other reactions, including clustering to form new particles. Other I_xO_y species have larger absorption cross sections in the actinic region, resulting in rapid photolysis to smaller iodine-containing molecules. Possible photolysis products include IO_3, which could be a precursor of HIO_3 in the marine boundary layer. These new findings highlight the need for new experimental and theoretical studies, particularly investigating the products of these photochemical processes, as well as the effect on IOP (and therefore cloud condensation nuclei) formation.

Appendix A: Molecular geometries and parameters of iodine oxides at the B3LYP/6-311+G(2d,p) (+AE) level of theory and benchmarking of the TD-DFT method for iodine oxides

Table A1. Molecular properties of I_2O_3, I_2O_4, I_3O_6 (cyclic), I_3O_6 (linear), I_3O_7 (cyclic), I_3O_7 (linear), IO_3, and the transition state for dissociation of IO_3 to $IO + O_2$ (illustrated in Fig. A1), and the stationary points on the $IO_3 + HO_2$ surface (Fig. 12).

Molecule	Cartesian co-ordinates/ Å*	Rotational constants/ GHz*	Vibrational frequencies/ cm$^{-1,}$*
I_2O_3	I, −0.009, −0.201, −0.192 O, −1.208, −0.160, 1.377 I, −0.583, 0.643, 3.128 O, 0.427, 1.521, −0.391 O, 1.423, −1.065, 0.438	4.46970, 0.57042, 0.55739	44, 88, 241, 256, 299, 450, 624, 872, 902
I_2O_4	O, −1.655, −0.203, 1.563 I, 0.046, 0.313, 1.770 O, 0.699, 0.048, −0.103 O, 0.936, −0.982, 2.619 I, −0.385, −0.913, −1.502 O, −1.272, 0.428, −2.370	3.55600, 0.49098, 0.47135	48, 67, 92, 164, 248, 260, 308, 444, 538, 812, 874, 906
I_3O_6 (cyclic)	I, 1.335, −1.791, −0.031 O, 1.569, 0.091, −0.823 O, 3.064, −2.228, 0.378 I, 1.319, 1.750, 0.186 O, −0.279, 1.411, 0.952 O, 1.051, 2.850, −1.192 I, −2.620, −0.026, 0.066 O, −1.412, −1.310, −0.437 O, −4.280, −0.729, −0.202	0.44642, 0.26455, 0.17279	18, 26, 54,59, 66, 70, 87, 107, 116, 171, 202, 274, 295, 319, 444, 563, 783, 804, 814, 843, 898
I_3O_6 (linear)	O, −0.860, 0.445, 0.841 I, −0.142, −0.977, −0.191 O, 1.698, −0.828, 0.694 O, −2.369, −1.079, −0.706 I, 3.054, 0.513, 0.198 O, 2.321, 1.165, −1.301 O, 4.415, −0.561, −0.236 I, −3.219, 0.313, 0.228 O, −3.185, 1.803, −0.797	1.40546, 0.15363, 0.14491	21, 33, 60, 69, 85, 98, 122, 166, 184, 262, 268, 302, 313, 343, 442, 565, 664, 699, 843, 871, 903
I_3O_7 (cyclic)	I, 1.050, −1.602, −0.490 O, 1.254, 1.127, −0.500 O, 1.159, −3.334, −0.902 I, 0.374, 2.634, 0.070 O, −1.810, 0.925, 0.501 O, 1.558, 4.011, −0.093 I, −2.237, −0.789, 0.151 O, 0.594, −1.505, 1.245 O, −3.595, −0.762, −1.001 O, −0.813, −1.235, −1.152	0.43718, 0.25525, 0.17036	29, 49, 61, 66, 79, 82, 90, 111, 123, 171, 186, 262, 279, 302, 308, 324, 494, 566, 782, 807, 852, 862, 905, 909

Table A1. Continued.

Molecule	Cartesian co-ordinates/ Å*	Rotational constants/ GHz*	Vibrational frequencies/ cm^{-1}*
I$_3$O$_7$ (linear)	O, 4.334, 1.318, 0.098 I, 3.552, −0.283, 0.217 O, 1.828, 0.194, 0.994 O, 2.970, −0.766, −1.411 I, 0.004, 0.013, 0.002 O, −1.823, −0.085, −0.997 O, 0.008, −1.794, 0.247 I, −3.543, −0.351, −0.118 O, −2.958, −0.382, 1.579 O, −4.337, 1.219, −0.426	2.11361, 0.11760, 0.11718	21, 25, 33, 44, 46, 60, 84, 140, 186, 203, 263, 266, 296, 312, 320, 418, 433, 552, 635, 759, 867, 867, 901, 902
IO$_3$	I, 0.080, 1.235, 0.000 O, 0.645, −0.481, 0.000 O, 0.645, 2.092, 1.486 O, 0.645, 2.092, −1.486	6.18204, 6.18204, 3.57497	258, 258, 268, 766, 766, 799
TS for IO$_3$ → IO + O$_2$	I, 0.205, 0.253, −0.082 O, 1.400, −1.046, 0.249 O, −1.406, −0.589, −0.790 O, −1.419, −0.181, 0.909	8.93231, 4.04781, 3.81028	−914, 142, 252, 354, 701, 867
IO$_3$−HO$_2$ complex	I, −0.649, 0.251, 0.072 O, −0.420, −1.455, 0.587 O, −0.429, 1.299, 1.501 O, 1.098, 0.455, −0.961 O, 2.104, −0.347, −0.326 O, 2.090, −1.626, −0.927 H, 1.449, −2.095, −0.357	4.44296, 1.49686, 1.34348	64, 143, 192, 226, 297, 316, 464, 530, 568, 719, 860, 903, 938, 1453, 3638
TS from IO$_3$ −complex to HIO$_3$ + O$_2$	I, 0.131, 1.178, −0.047 O, 0.550, −0.594, 0.341 O, 0.383, 2.058, 1.482 O, 1.579, 1.575, −1.172 O, 2.931, 0.475, −0.440 O, 2.661, −0.726, −0.774 H, 1.671, −0.878, −0.163	4.24271, 1.59293, 1.46409	1000i, 74, 225, 250, 288, 323, 377, 500, 624, 711, 823, 904, 1246, 1306, 1749
HIO$_3$	I, 1.574, −0.480, 0.151 O, −0.137, −0.710, −0.315 O, 2.309, 0.401, −1.439 O, 1.647, 0.832, 1.363 H, 1.792, 1.203, −1.629	5.68293, 5.36595, 3.62995	62, 258, 274, 304, 584, 871, 901, 981, 3732

* Calculated at the B3LYP/gen level of theory (see text).

Table A2. Peak wavelengths and oscillator strengths (f) for the first 30 excited states of HOI, IO, OIO, and IO_3 at the TD/B3LYP/G2 level of theory.

HOI		IO		OIO		IO_3	
λ/nm	f	λ/nm	f	λ/nm	f	λ/nm	f
450.3	0.0001	94003.7	0	598.9	0	1378.3	0
367.0	0.0027	513.0	0	586.8	0.0002	951.7	0.0039
224.7	0.0089	390.6	0	584.2	0.0217	951.0	0.0039
192.8	0.0478	386.7	0.0001	342.6	0.0006	719.7	0.0081
178.4	0.0999	379.4	0.0365	337.5	0	719.3	0.0081
173.3	0.072	338.5	0.0001	281.0	0	264.4	0.0027
168.9	0.1978	321.0	0.0001	278.7	0	264.4	0.0027
165.4	0.0447	244.5	0.0052	270.3	0.0027	254.9	0.0127
164.9	0.002	230.9	0.0001	262.6	0	249.4	0
161.4	0.0659	212.4	0.0006	262.0	0	246.4	0.0001
157.9	0.0003	198.7	0.0114	249.7	0.0046	246.3	0.0001
153.2	0.0056	193.5	0.0249	247.5	0.0002	237.2	0.011
139.2	0.082	185.3	0.085	232.7	0.0009	222.1	0.001
133.4	0.0191	179.6	0.0112	231.1	0.0008	222.0	0.001
131.4	0.1567	173.2	0	229.9	0	221.5	0
130.7	0.0911	172.9	0.009	228.1	0.0459	213.8	0.0029
121.7	0.0214	167.4	0	219.8	0.0002	213.7	0.0028
121.4	0.071	167.3	0.0642	206.5	0	205.0	0
118.8	0.0341	165.8	0.02	200.6	0.0063	205.0	0
118.6	0.0023	163.6	0.0007	188.6	0.0279	197.4	0.0013
117.2	0.0009	157.9	0.0005	173.8	0.1771	195.2	0.0019
116.0	0.0059	152.0	0.037	167.5	0.0123	195.2	0.0019
114.9	0.067	150.7	0	167.2	0.0064	193.9	0.0076
112.3	0.0094	143.6	0	166.4	0.0007	193.8	0.0075
112.0	0	142.0	0.0836	165.4	0	192.3	0
111.0	0.037	140.5	0.4635	164.6	0	190.2	0.0085
110.3	0.0068	131.0	0	162.0	0.0002	190.2	0.0083
109.3	0.073	130.9	0.0107	155.5	0	187.1	0.015
105.8	0.0404	130.1	0.0358	155.1	0.0004	186.3	0
105.4	0.4533	126.0	0.0663	155.0	0.0017	185.0	0.0145

Table A3. Peak wavelengths and oscillator strengths (f) for the first 30 excited states of I_2O_2, I_2O_3, and I_2O_4 at the TD/B3LYP/G2 level of theory.

I_2O_2		I_2O_3		I_2O_4	
λ/nm	f	λ/nm	f	λ/nm	f
758.1	0.0063	518.9	0	676.5	0.0051
563.0	0	455.5	0.0045	366.0	0.0039
480.6	0.0062	335.2	0.034	344.7	0.0008
367.6	0.0052	334.6	0.0006	323.6	0.0348
338.9	0.0108	297.5	0.0046	319.4	0.0375
306.4	0.0478	286.1	0.0025	291.7	0.0342
300.0	0.0009	265.6	0.0061	287.3	0.0017
275.3	0.0358	258.6	0.0419	280.1	0.079
270.3	0.0047	240.7	0.0532	267.9	0.0085
257.1	0.0163	236.0	0.0009	253.3	0.0124
255.4	0.0017	229.0	0.0068	248.1	0.0082
252.7	0.1031	227.5	0	241.0	0.0058
226.1	0.0106	225.7	0.002	237.0	0.0116
219.1	0.0049	223.6	0.0002	231.6	0.0059
200.2	0.0081	217.4	0.0005	228.1	0.0086
199.3	0.0406	215.7	0.0129	225.9	0.001
192.8	0.0187	214.7	0.0169	218.9	0.0145
186.8	0.0034	211.4	0.0039	216.4	0.0101
184.6	0.0041	209.0	0.0332	213.8	0.0181
184.1	0.009	200.7	0.0183	209.6	0.0124
179.0	0.0667	199.1	0.0019	207.6	0.002
177.8	0.0844	197.1	0.1393	206.8	0.0026
177.4	0.0251	190.5	0.0454	202.3	0.0031
172.6	0.0911	185.7	0.0031	199.1	0.0044
170.0	0.0251	175.2	0.0321	197.3	0.0016
168.5	0.007	174.6	0.0031	196.3	0.0101
165.2	0.0301	170.2	0.1018	194.1	0.0283
162.7	0.0146	169.6	0.0256	193.7	0.0071
162.1	0.0058	168.9	0.062	191.9	0.0036
161.2	0.091	167.3	0	190.3	0.0036

Table A4. Peak wavelengths and oscillator strengths (f) for the first 30 excited states of I_3O_6 linear, I_3O_6 cyclic, I_3O_7 linear, and I_3O_7 cyclic at the TD/B3LYP/G2 level of theory.

I_3O_6 linear		I_3O_6 cyclic		I_3O_7 linear		I_3O_7 cyclic	
λ/nm	f	λ/nm	f	λ/nm	f	λ/nm	f
1010.2	0.0052	1235.0	0	880.9	0.0002	643.1	0.0001
554.6	0.0095	850.6	0.0067	782.1	0.0005	546.0	0.0287
486.0	0.0242	771.7	0.0023	657.6	0.0001	517.8	0.0002
467.9	0.0005	630.7	0.0001	606.3	0.0001	434.1	0.0022
452.6	0.0123	550.4	0.0229	601.9	0.0007	427.1	0.0003
432.5	0.0002	531.2	0.0001	542.8	0.002	389.5	0.0014
424.1	0.0032	518.5	0	529.3	0.0006	386.1	0.0002
416.0	0.014	462.3	0.0001	490.3	0.0089	364.3	0.0004
403.2	0.0047	433.1	0	479.5	0.005	357.1	0.0002
390.8	0.0033	392.7	0.0004	462.5	0.0089	355.6	0.0001
384.2	0.004	387.8	0.0082	382.9	0.0054	351.9	0.002
379.0	0.0031	371.9	0.0002	376.9	0.0006	347.7	0.0005
361.9	0.0203	363.2	0	364.0	0.001	343.5	0.012
353.4	0.0154	354.1	0.0008	353.5	0	338.7	0.0042
347.0	0.0009	351.2	0.0013	340.1	0.0052	334.2	0.0039
344.8	0.0159	349.1	0.0002	333.9	0.0004	331.7	0.0108
336.5	0.0117	339.8	0.0023	331.7	0.0032	329.8	0.0001
329.5	0.0073	333.3	0.0001	311.0	0	326.3	0.001
323.7	0.0024	332.1	0	305.6	0.082	322.0	0.0022
321.8	0.0044	325.4	0.0026	304.5	0.0737	320.2	0.0026
317.7	0.0015	325.0	0.0009	300.9	0.0001	314.1	0.0019
316.2	0.0079	323.1	0.0017	295.3	0.0005	310.1	0.0031
301.6	0.0035	318.5	0.0081	290.8	0.0013	302.7	0.0004
297.6	0.0115	315.8	0.008	290.2	0.0013	298.5	0.0003
295.8	0.002	311.9	0.0028	289.9	0.0028	297.4	0.0007
295.1	0.0234	309.0	0.0521	284.9	0.0055	293.3	0.0015
290.2	0.0001	308.0	0.0011	279.1	0.0005	292.6	0.0004
284.7	0.0015	306.2	0.0015	275.3	0	289.0	0.004
282.3	0.0102	302.8	0.0014	274.8	0.0018	285.4	0.0034
279.0	0.0059	299.0	0.0014	269.4	0.0003	282.2	0.0025
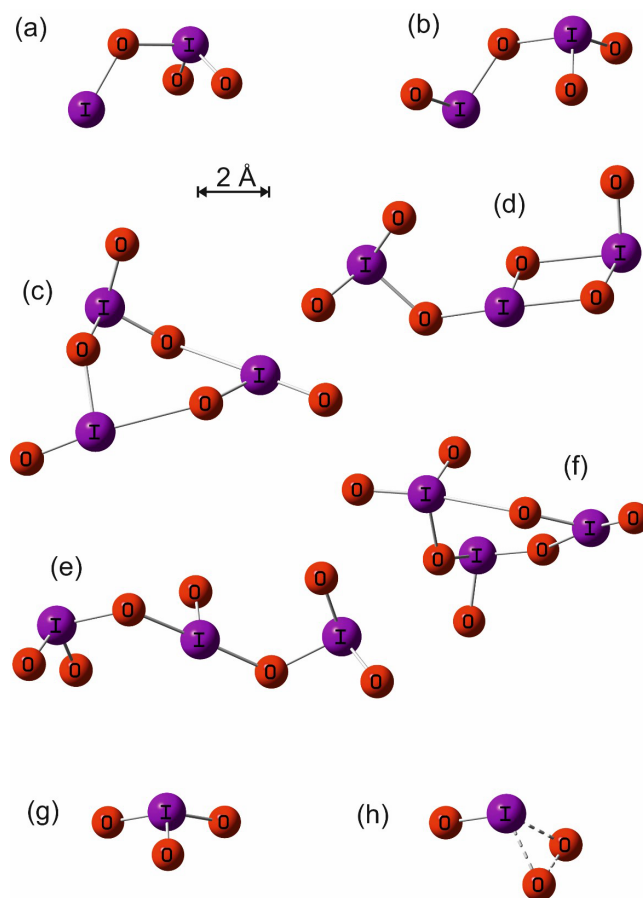
Figure A1. Molecular geometries of I_2O_3, I_2O_4, I_3O_6 (cyclic), I_3O_6 (linear), I_3O_7 (cyclic), I_3O_7 (linear), IO_3, and the transition state for dissociation of IO_3 to $IO + O_2$, calculated at the B3LYP/gen level of theory (see main text for details).
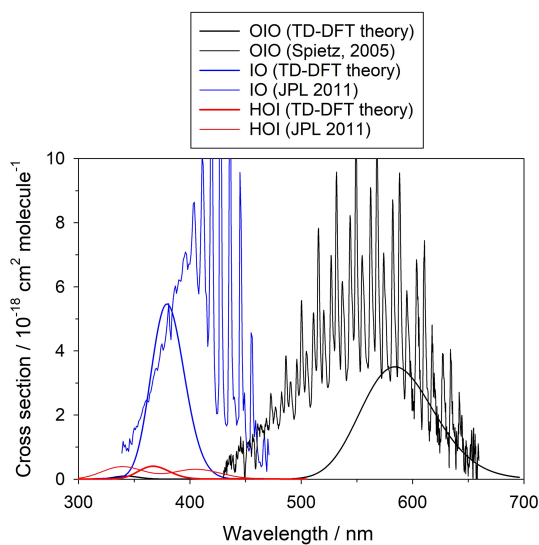

Figure A2. Experimental absorption cross sections of IO (Sander et al., 2011), OIO (Spietz et al., 2005), and HOI (Sander et al., 2011) and absorption spectra calculated with the TD-DFT method (this work).

Appendix B: Photofragmentation of I_xO_y species

The photofragmentation of I_xO_y species to product ions in the photoionization chamber of the detection apparatus necessitates careful experimentation in order to ensure that any photodepletion of a species of interest is solely due to its 355 or 532 nm photolysis in the flow tube and not obscured by the product ions of larger I_xO_y species. To elucidate the optimal window for investigating photodepletion of each species, time-resolved mass spectra were recorded for each set of experimental conditions (Fig. 5). From the kinetic information, it is then possible to inspect the averages of the mass spectra within these windows to ensure that the species of interest is present, but larger I_xO_y species are not, as shown in Fig. B1. By ensuring no larger I_xO_y species are present, it follows that for a species of interest, only precursor ions of the species are contributing to the signal intensity within that time window, and that no contribution to the recorded signal is coming from product ions. Note that the signals shown in Figs. 5 and B1 are not accumulated for extended periods of time and as such are relatively noisy. Long accumulation times and corresponding large signal-to-noise ratios are unnecessary for these experiments, since the objective is simply to elucidate optimal time delays within which photodepletion experiments are carried out (photodepletion experiments are typically carried out for $\sim 10\times$ as many accumulations) and are carried out prior to an experimental session. It should be noted also that the optimal timescales such as those shown in Fig. 5 and Figure B1 vary depending on the concentration of IO formed at the beginning of the reaction sequence, and since the reactions which facilitate the stepwise formation of the higher oxides are second order, even modest changes in [IO] at early times can result in significant changes to the appearance times of the different species of interest.
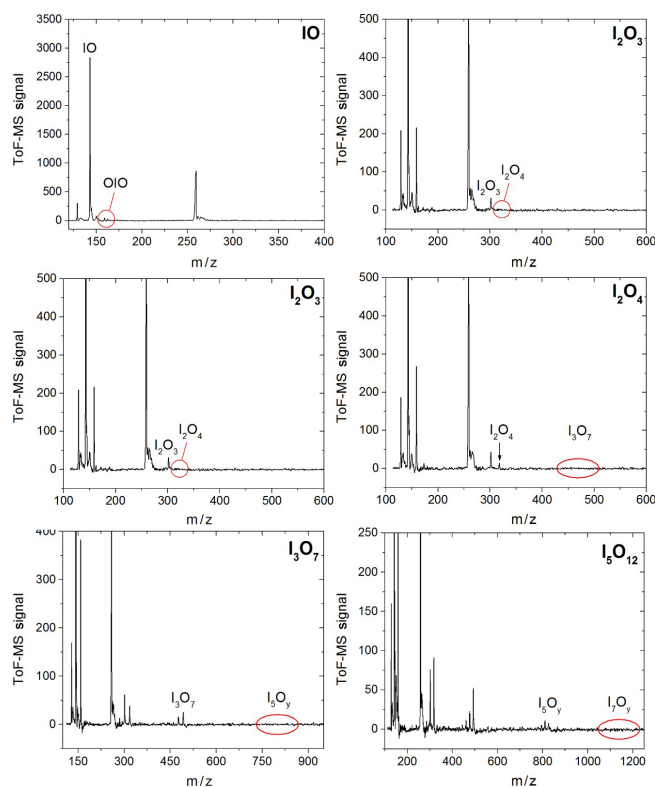

Figure B1. Mass spectra corresponding to the optimized time delays shown in Fig. 5. The plots are generated by averaging the signal obtained for each mass over the 5 ms window. The species of interest is given in the top right corner of each spectrum.

References

Ashworth, S. H., Allan, B. J., and Plane, J. M. C.: High resolution spectroscopy of the OIO radical: Implications for the ozone-depleting potential of iodine, Geophys. Res. Lett., 29, 1456, https://doi.org/10.1029/2001gl013851, 2002.

Atkinson, R., Baulch, D. L., Cox, R. A., Crowley, J. N., Hampson, R. F., Hynes, R. G., Jenkin, M. E., Rossi, M. J., and Troe, J.: Evaluated kinetic and photochemical data for atmospheric chemistry: Volume III – gas phase reactions of inorganic halogens, Atmos. Chem. Phys., 7, 981–1191, https://doi.org/10.5194/acp-7-981-2007, 2007.

Baeza-Romero, M. T., Blitz, M. A., Goddard, A., and Seakins, P. W.: Time-of-flight mass spectrometry for time-resolved measurements: Some developments and applications, Int. J. Chem. Kinet., 44, 532–545, https://doi.org/10.1002/kin.20620, 2012.

Bloss, W. J., Rowley, D. M., Cox, R. A., and Jones, R. L.: Kinetics and Products of the IO Self-Reaction, J. Phys. Chem. A, 105, 7840–7854, https://doi.org/10.1021/jp0044936, 2001.

Burkholder, J. B., Sander, S. P., Abbat, J., Barker, J. R., Huie, R. E., Kolb, C. E., Kurylo, M. J., Orkin, V. L., Wilmouth, D. M., and Wine, P. H.: Chemical Kinetics and Photochemical Data for Use in Atmospheric Studies, Evaluation No. 18 JPL-NASA, Pasadena, 2015.

Burrows, J., Richter, A., Dehn, A., Deters, B., Himmelmann, S., Voigt, S., and Orphal, J.: Atmospheric remote-sensing reference data from GOME – 2. Temperature-dependent absorption cross sections of O_3 in the 231–794 nm range, J. Quant. Spectrosc. Ra., 61, 509–517, https://doi.org/10.1016/S0022-4073(98)00037-5, 1999.

Canneaux, S., Xerri, B., Louis, F., and Cantrel, L.: Theoretical Study of the Gas-Phase Reactions of Iodine Atoms ($^2P_{3/2}$) with H_2, H_2O, HI, and OH, J. Phys. Chem. A, 114, 9270–9288, https://doi.org/10.1021/jp104163t, 2010.

Carpenter, L. J., MacDonald, S. M., Shaw, M. D., Kumar, R., Saunders, R. W., Parthipan, R., Wilson, J., and Plane, J. M. C.: Atmospheric iodine levels influenced by sea surface emissions of inorganic iodine, Nat. Geosci., 6, 108–111, https://doi.org/10.1038/ngeo1687, 2013.

Chance, R., Baker, A. R., Carpenter, L., and Jickells, T. D.: The distribution of iodide at the sea surface, Environ. Sci. Process Impacts, 16, 1841–1859, https://doi.org/10.1039/c4em00139g, 2014.

Cox, R. A. and Coker, G. B.: Absorption Cross section and Kinetics of IO in the Photolysis of CH_3I in the presence of Ozone, J. Phys. Chem., 87, 4478–4484, https://doi.org/10.1021/j100245a030, 1983.

Cuevas, C. A., Maffezzoli, N., Corella, J. P., Spolaor, A., Vallelonga, P., Kjær, H. A., Simonsen, M., Winstrup, M., Vinther, B., Horvat, C., Fernandez, R. P., Kinnison, D., Lamarque, J.-F., Barbante, C., and Saiz-Lopez, A.: Rapid increase in atmospheric iodine levels in the North Atlantic since the mid-20th century, Nat. Commun., 9, 1452, https://doi.org/10.1038/s41467-018-03756-1, 2018.

Dennington, R., Keith, T. A., and Millam, J. M.: GaussView, Version 6.1, Semichem Inc., Shawnee Mission, KS, 2016.

Fernandez, R. P., Salawitch, R. J., Kinnison, D. E., Lamarque, J.-F., and Saiz-Lopez, A.: Bromine partitioning in the tropical tropopause layer: implications for stratospheric injection, Atmos. Chem. Phys., 14, 13391–13410, https://doi.org/10.5194/acp-14-13391-2014, 2014.

Foresman, J. B. and Frisch, Æ.: Exploring Chemistry with Electronic Structure Methods 3rd. Ed., Gaussian, Inc., Wallingford, CT, USA, 2015.

Frisch, M. J., Trucks, G. W., Schlegel, H. B., Scuseria, G. E., Robb, M. A., Cheeseman, J. R., Scalmani, G., Barone, V., Petersson, G. A., Nakatsuji, H., Li, X., Caricato, M., Marenich, A. V., Bloino, J., Janesko, B. G., Gomperts, R., Mennucci, B., Hratchian, H. P., Ortiz, J. V., Izmaylov, A. F., Sonnenberg, J. L., Williams-Young, D., Ding, F., Lipparini, F., Egidi, F., Goings, J., Peng, B., Petrone, A., Henderson, T., Ranasinghe, D., Zakrzewski, V. G., J. Gao, N. R., Zheng, G., Liang, W., Hada, M., Ehara, M., Toyota, K., Fukuda, R., Hasegawa, J., Ishida, M., Nakajima, T., Honda, Y., Kitao, O., Nakai, H., Vreven, T., Throssell, K., J. A. Montgomery, J., Peralta, J. E., Ogliaro, F., Bearpark, M. J., Heyd, J. J., Brothers, E. N., Kudin, K. N., Staroverov, V. N., Keith, T. A., Kobayashi, R., Normand, J., Raghavachari, K., Rendell, A. P., Burant, J. C., Iyengar, S. S., Tomasi, J., Cossi, M., Millam, J. M., Klene, M., Adamo, C., Cammi, R., Ochterski, J. W., Martin, R. L., Morokuma, K., Farkas, O., Foresman, J. B., and Fox, D.

J.: Gaussian 16, Revision B.01, Gaussian, Inc., Wallingford, CT, USA, 2016.

Galvez, O., Gómez Martín, J. C., Gomez, P. C., Saiz-Lopez, A., and Pacios, L. F.: A theoretical study on the formation of iodine oxide aggregates and monohydrates, Phys. Chem. Chem. Phys., 15, 15572–15583, https://doi.org/10.1039/c3cp51219c, 2013.

Glowacki, D. R., Liang, C.-H., Morley, C., Pilling, M. J., and Robertson, S. H.: MESMER: An Open-Source Master Equation Solver for Multi-Energy Well Reactions, J. Phys. Chem. A, 116, 9545–9560, https://doi.org/10.1021/jp3051033, 2012.

Glukhovtsev, M. N., Pross, A., McGrath, M. P., and Radom, L.: Extension of Gaussian-2 (G2) theory to bromine- and iodine-containing molecules: Use of effective core potentials, J. Chem. Phys., 103, 1878–1885, https://doi.org/10.1063/1.469712, 1995.

Gómez Martín, J. C., Spietz, P., and Burrows, J. P.: Spectroscopic studies of the I_2/O_3 photochemistry: Part 1: Determination of the absolute absorption cross sections of iodine oxides of atmospheric relevance, J. Photoch. Photobio., A, 176, 15–38, https://doi.org/10.1016/j.jphotochem.2005.09.024, 2005.

Gómez Martín, J. C., Spietz, P., and Burrows, J. P.: Kinetic and Mechanistic Studies of the I_2/O_3 Photochemistry, J. Phys. Chem. A, 111, 306–320, https://doi.org/10.1021/jp061186c, 2007.

Gómez Martín, J. C., Ashworth, S. H., Mahajan, A. S., and Plane, J. M. C.: Photochemistry of OIO: Laboratory study and atmospheric implications, Geophys. Res. Lett., 36, L09802, https://doi.org/10.1029/2009GL037642, 2009.

Gómez Martín, J. C., Galvez, O., Baeza-Romero, M. T., Ingham, T., Plane, J. M. C., and Blitz, M. A.: On the mechanism of iodine oxide particle formation, Phys. Chem. Chem. Phys., 15, 15612–15622, https://doi.org/10.1039/c3cp51217g, 2013.

Gómez Martín, J. C., Garraway, S. A., and Plane, J. M. C.: Reaction Kinetics of Meteoric Sodium Reservoirs in the Upper Atmosphere, J. Phys. Chem. A, 120, 1330–1346, https://doi.org/10.1021/acs.jpca.5b00622, 2016.

Gómez Martín, J. C., Lewis, T., Blitz, M. A., Plane, J. M., Kumar, M., Francisco, J. S., and Saiz-Lopez, A.: A gas-to-particle conversion mechanism helps to explain atmospheric particle formation through clustering of iodine oxides, Nat. Commun., 11, 4521, https://doi.org/10.1038/s41467-020-18252-8, 2020.

Hammaecher, C., Canneaux, S., Louis, F., and Cantrel, L.: A Theoretical Study of the H-Abstraction Reactions from HOI by Moist Air Radiolytic Products (H, OH, and $O(^3P)$) and Iodine Atoms ($^2P_{3/2}$), J. Phys. Chem. A, 115, 6664–6674, https://doi.org/10.1021/jp202760u, 2011.

Harwood, M. H., Burkholder, J. B., Hunter, M., Fox, R. W., and Ravishankara, A. R.: Absorption Cross Sections and Self-Reaction Kinetics of the IO Radical, J. Phys. Chem. A, 101, 853–863, https://doi.org/10.1021/jp962429b, 1997.

Hoffmann, T., O'Dowd, C. D., and Seinfeld, J. H.: Iodine oxide homogeneous nucleation: An explanation for coastal new particle production, Geophys. Res. Lett., 28, 1949–1952, https://doi.org/10.1029/2000GL012399, 2001.

Jimenez, J. L., Bahreini, R., Cocker, D. R., III, Zhuang, H., Varutbangkul, V., Flagan, R. C., Seinfeld, J. H., O'Dowd, C. D., and Hoffmann, T.: New particle formation from photooxidation of diiodomethane (CH_2I_2), J. Geophys. Res.-Atmos., 108, 4318, https://doi.org/10.1029/2002JD002452, 2003.

Joseph, D. M., Ashworth, S. H., and Plane, J. M. C.: The absorption cross-section and photochemistry of OIO, J. Photoch. Photobio. A, 176, 68–77, https://doi.org/10.1016/j.jphotochem.2005.09.003, 2005.

Kaltsoyannis, N. and Plane, J. M. C.: Quantum chemical calculations on a selection of iodine-containing species (IO, OIO, INO_3, $(IO)_2$, I_2O_3, I_2O_4 and I_2O_5) of importance in the atmosphere, Phys. Chem. Chem. Phys., 10, 1723–1733, https://doi.org/10.1039/b715687c, 2008.

Khanniche, S., Louis, F., Cantrel, L., and Černušák, I.: Thermochemistry of HIO_2 Species and Reactivity of Iodous Acid with OH Radical: A Computational Study, ACS Earth Space Chem., 1, 39–49, https://doi.org/10.1021/acsearthspacechem.6b00010, 2017a.

Khanniche, S., Louis, F., Cantrel, L., and Černušák, I.: Investigation of the Reaction Mechanism and Kinetics of Iodic Acid with OH Radical Using Quantum Chemistry, ACS Earth Space Chem., 1, 227–235, https://doi.org/10.1021/acsearthspacechem.7b00038, 2017b.

Koenig, T. K., Baidar, S., Campuzano-Jost, P., Cuevas, C. A., Dix, B., Fernandez, R. P., Guo, H., Hall, S. R., Kinnison, D., Nault, B. A., Ullmann, K., Jimenez, J. L., Saiz-Lopez, A., and Volkamer, R.: Quantitative detection of iodine in the stratosphere, P. Natl. Acad. Sci. USA, 117, 1860–1866, https://doi.org/10.1073/pnas.1916828117, 2020.

Kumar, M., Saiz-Lopez, A., and Francisco, J. S.: Single-Molecule Catalysis Revealed: Elucidating the Mechanistic Framework for the Formation and Growth of Atmospheric Iodine Oxide Aerosols in Gas-Phase and Aqueous Surface Environments, J. Am. Chem. Soc., 140, 14704–14716, https://doi.org/10.1021/jacs.8b07441, 2018.

Kung, A. H., Young, J. F., and Harris, S. E.: Generation of 1182-Å radiation in phase-matched mixtures of inert gases, Appl. Phys. Lett., 22, 301–302, https://doi.org/10.1063/1.1654647, 1973.

Lamarque, J.-F., Emmons, L. K., Hess, P. G., Kinnison, D. E., Tilmes, S., Vitt, F., Heald, C. L., Holland, E. A., Lauritzen, P. H., Neu, J., Orlando, J. J., Rasch, P. J., and Tyndall, G. K.: CAM-chem: description and evaluation of interactive atmospheric chemistry in the Community Earth System Model, Geosci. Model Dev., 5, 369–411, https://doi.org/10.5194/gmd-5-369-2012, 2012.

Laszlo, B., Kurylo, M. J., and Huie, R. E.: Absorption cross sections, kinetics of formation, and self-reaction of the IO radical produced via the laser photolysis of $N_2O/I_2/N_2$ mixtures, J. Phys. Chem., 99, 11701–11707, https://doi.org/10.1021/j100030a013, 1995.

Lewis, T., Heard, D. E., and Blitz, M. A.: A novel multiplex absorption spectrometer for time-resolved studies, Rev. Sci. Instrum., 89, 024101, https://doi.org/10.1063/1.5006539, 2018.

MacDonald, S. M., Gómez Martín, J. C., Chance, R., Warriner, S., Saiz-Lopez, A., Carpenter, L. J., and Plane, J. M. C.: A laboratory characterisation of inorganic iodine emissions from the sea surface: dependence on oceanic variables and parameterisation for global modelling, Atmos. Chem. Phys., 14, 5841-5852, https://doi.org/10.5194/acp-14-5841-2014, 2014.

Mahon, R., McIlrath, T., Myerscough, V., and Koopman, D.: Third-harmonic generation in argon, krypton, and xenon: Bandwidth limitations in the vicinity of Lyman-α, IEEE J. Quantum Elect., 15, 444–451, https://doi.org/10.1109/jqe.1979.1070036, 1979.

McFiggans, G., Coe, H., Burgess, R., Allan, J., Cubison, M., Alfarra, M. R., Saunders, R., Saiz-Lopez, A., Plane, J. M. C., Wevill, D., Carpenter, L., Rickard, A. R., and Monks, P. S.: Direct evidence for coastal iodine particles from Laminaria macroalgae – linkage to emissions of molecular iodine, Atmos. Chem. Phys., 4, 701–713, https://doi.org/10.5194/acp-4-701-2004, 2004.

Ordóñez, C., Lamarque, J.-F., Tilmes, S., Kinnison, D. E., Atlas, E. L., Blake, D. R., Sousa Santos, G., Brasseur, G., and Saiz-Lopez, A.: Bromine and iodine chemistry in a global chemistry-climate model: description and evaluation of very short-lived oceanic sources, Atmos. Chem. Phys., 12, 1423–1447, https://doi.org/10.5194/acp-12-1423-2012, 2012.

Peterson, K. A.: A theoretical study of the low-lying electronic states of OIO and the ground states of IOO and OIO-, Mol. Phys., 108, 393–408, https://doi.org/10.1080/00268970903508548, 2010.

Pirjola, L., O'Dowd, C., Yoon, Y. J., and Sellegri, K.: Modelling Iodine Particle Formation and Growth from Seaweed in a Chamber, Environ. Chem., 2, 271–281, https://doi.org/10.1071/EN05075, 2005.

Prados-Roman, C., Cuevas, C. A., Fernandez, R. P., Kinnison, D. E., Lamarque, J.-F., and Saiz-Lopez, A.: A negative feedback between anthropogenic ozone pollution and enhanced ocean emissions of iodine, Atmos. Chem. Phys., 15, 2215–2224, https://doi.org/10.5194/acp-15-2215-2015, 2015.

Saiz-Lopez, A. and Plane, J. M. C.: Novel iodine chemistry in the marine boundary layer, Geophys. Res. Lett., 31, L04112, https://doi.org/10.1029/2003GL019215, 2004.

Saiz-Lopez, A., Saunders, R. W., Joseph, D. M., Ashworth, S. H., and Plane, J. M. C.: Absolute absorption cross-section and photolysis rate of I$_2$, Atmos. Chem. Phys., 4, 1443–1450, https://doi.org/10.5194/acp-4-1443-2004, 2004.

Saiz-Lopez, A., Lamarque, J.-F., Kinnison, D. E., Tilmes, S., Ordóñez, C., Orlando, J. J., Conley, A. J., Plane, J. M. C., Mahajan, A. S., Sousa Santos, G., Atlas, E. L., Blake, D. R., Sander, S. P., Schauffler, S., Thompson, A. M., and Brasseur, G.: Estimating the climate significance of halogen-driven ozone loss in the tropical marine troposphere, Atmos. Chem. Phys., 12, 3939–3949, https://doi.org/10.5194/acp-12-3939-2012, 2012a.

Saiz-Lopez, A., Plane, J. M., Baker, A. R., Carpenter, L. J., von Glasow, R., Martin, J. C., McFiggans, G., and Saunders, R. W.: Atmospheric chemistry of iodine, Chem. Rev., 112, 1773–1804, https://doi.org/10.1021/cr200029u, 2012b.

Saiz-Lopez, A., Fernandez, R. P., Ordóñez, C., Kinnison, D. E., Gómez Martín, J. C., Lamarque, J.-F., and Tilmes, S.: Iodine chemistry in the troposphere and its effect on ozone, Atmos. Chem. Phys., 14, 13119–13143, https://doi.org/10.5194/acp-14-13119-2014, 2014.

Saiz-Lopez, A., Baidar, S., Cuevas, C. A., Koenig, T., Fernandez, R. P., Dix, B., Kinnison, D. E., Lamarque, J.-F., Rodriguez-Lloveras, X., and Campos, T. L.: Injection of iodine to the stratosphere, Geophys. Res. Lett., 42, 6852–6859, https://doi.org/10.1002/2015GL064796, 2015.

Sander, S. P., Abbatt, J., Barker, J. R., Burkholder, J. B., Friedl, R. R., Golden, D. M., Huie, R. E., Kolb, C. E., Kurylo, M. J., Moortga, G. K., Orkin, V. L., and Wine, P. H.: Chemical Kinetics and Photochemical Data for Use in Atmospheric Studies, Evaluation Number 17, Jet Propulsion Laboratory, Pasadena, USA, 2011.

Saunders, R. W., Mahajan, A. S., Gómez Martín, J. C., Kumar, R., and Plane, J. M. C.: Studies of the Formation and Growth of Aerosol from Molecular Iodine Precursor, Z. Phys. Chem., 224, 1095–1117, https://doi.org/10.1524/zpch.2010.6143, 2010.

Sherwen, T., Evans, M. J., Carpenter, L. J., Andrews, S. J., Lidster, R. T., Dix, B., Koenig, T. K., Sinreich, R., Ortega, I., Volkamer, R., Saiz-Lopez, A., Prados-Roman, C., Mahajan, A. S., and Ordóñez, C.: Iodine's impact on tropospheric oxidants: a global model study in GEOS-Chem, Atmos. Chem. Phys., 16, 1161–1186, https://doi.org/10.5194/acp-16-1161-2016, 2016.

Sipilä, M., Sarnela, N., Jokinen, T., Henschel, H., Junninen, H., Kontkanen, J., Richters, S., Kangasluoma, J., Franchin, A., Peräkylä, O., Rissanen, M. P., Ehn, M., Vehkamäki, H., Kurten, T., Berndt, T., Petäjä, T., Worsnop, D., Ceburnis, D., Kerminen, V.-M., Kulmala, M., and O'Dowd, C.: Molecular-scale evidence of aerosol particle formation via sequential addition of HIO$_3$, Nature, 537, 532–534, https://doi.org/10.1038/nature19314, 2016.

Spietz, P., Gómez Martín, J. C., and Burrows, J. P.: Spectroscopic studies of the I$_2$/O$_3$ photochemistry: Part 2. Improved spectra of iodine oxides and analysis of the IO absorption spectrum, J. Photoch. Photobio. A, 176, 50–67, https://doi.org/10.1016/j.jphotochem.2005.08.023, 2005.

Stone, D., Whalley, L. K., and Heard, D. E.: Tropospheric OH and HO$_2$ radicals: field measurements and model comparisons, Chem. Soc. Rev., 41, 6348–6404, https://doi.org/10.1039/c2cs35140d, 2012.

Stratmann, R. E., Scuseria, G. E., and Frisch, M. J.: An efficient implementation of time-dependent density-functional theory for the calculation of excitation energies of large molecules, J. Chem. Phys., 109, 8218–8224, https://doi.org/10.1063/1.477483, 1998.

Tucceri, M. E., Hölscher, D., Rodriguez, A., Dillon, T. J., and Crowley, J. N.: Absorption cross section and photolysis of OIO, Phys. Chem. Chem. Phys., 8, 834–846, https://doi.org/10.1039/b512702e, 2006.

Vandaele, A. C., Hermans, C., Simon, P. C., Carleer, M., Colin, R., Fally, S., Mérienne, M. F., Jenouvrier, A., and Coquart, B.: Measurements of the NO$_2$ absorption cross-section from $42\,000\,cm^{-1}$ to $10\,000\,cm^{-1}$ (238–1000 nm) at $220\,K$ and $294\,K$, J. Quant. Spectrosc. Ra., 59, 171–184, https://doi.org/10.1016/S0022-4073(97)00168-4, 1998.

Wei, N., Hu, C., Zhou, S., Ma, Q., Mikuška, P., Večeřa, Z., Gai, Y., Lin, X., Gu, X., Zhao, W., Fang, B., Zhang, W., Chen, J., Liu, F., Shan, X., and Sheng, L.: VUV photoionization aerosol mass spectrometric study on the iodine oxide particles formed from O$_3$-initiated photooxidation of diiodomethane (CH$_2$I$_2$), RSC Adv., 7, 56779–56787, https://doi.org/10.1039/c7ra11413c, 2017.